An efficient method to calculate depth-integrated, phase-averaged momentum balances in non-hydrostatic models

da Silva, Renan F.; Rijnsdorp, Dirk P.; Hansen, Jeff E.; Lowe, Ryan; Buckley, Mark; Zijlema, Marcel

DOI
10.1016/j.ocemod.2021.101846

Publication date
2021

Document Version
Final published version

Published in
Ocean Modelling

Citation (APA)
da Silva, R. F., Rijnsdorp, D. P., Hansen, J. E., Lowe, R., Buckley, M., & Zijlema, M. (2021). An efficient method to calculate depth-integrated, phase-averaged momentum balances in non-hydrostatic models. *Ocean Modelling*, *165*, Article 101846. https://doi.org/10.1016/j.ocemod.2021.101846

Ocean Modelling 165 (2021) 101846

Contents lists available at ScienceDirect

Ocean Modelling

journal homepage: www.elsevier.com/locate/ocemod

An efficient method to calculate depth-integrated, phase-averaged momentum balances in non-hydrostatic models

Renan F. da Silva [a,b,c,d,*], Dirk P. Rijnsdorp [b,c,e,f,h], Jeff E. Hansen [a,b,c,e], Ryan Lowe [a,b,c,d,e], Mark Buckley [g], Marcel Zijlema [h]

[a] School of Earth Sciences, The University of Western Australia, Crawley, WA 6009, Australia
[b] UWA Oceans Institute, The University of Western Australia, Crawley, WA 6009, Australia
[c] Wave Energy Research Centre, The University of Western Australia, Albany Centre, Albany, WA 6330, Australia
[d] ARC Centre of Excellence for Coral Reef Studies, The University of Western Australia, Crawley, WA, 6009, Australia
[e] Oceans Graduate School, The University of Western Australia, Crawley, WA 6009, Australia
[f] Centre for Offshore Foundation Systems, The University of Western Australia, Crawley, WA 6009, Australia
[g] U.S. Geological Survey, St. Petersburg Coastal and Marine Science Center, St. Petersburg, FL 33701, USA
[h] Environmental Fluid Mechanics Section, Faculty of Civil Engineering and Geosciences, Delft University of Technology, 2600 GA Delft, The Netherlands

ARTICLE INFO

Keywords:
Momentum balance
Wave-induced flow
Surf zone
Wave modelling
Non-hydrostatic
SWASH

ABSTRACT

Analysis of the mean (wave-averaged) momentum balance is a common approach used to explain the physical forcing driving wave set-up and mean currents in the nearshore zone. Traditionally this approach has been applied to phase-averaged models but has more recently been applied to phase-resolving models using post-processing, whereby model output is used to calculate each of the momentum terms. While phase-resolving models have the advantage of capturing the nonlinear properties of waves propagating in the nearshore (making them advantageous to enhance understanding of nearshore processes), the post-processing calculation of the momentum terms does not guarantee that the momentum balance closes. We show that this is largely due to the difficulty (or impossibility) of being consistent with the numerical approach. If the residual is of a similar magnitude as any of the relevant momentum terms (which is common with post-processing methods as we show), the analysis is largely compromised. Here we present a new method to internally calculate and extract the depth-integrated, mean momentum terms in the phase-resolving non-hydrostatic wave-flow model SWASH in a manner that is consistent with the numerical implementation. Further, we demonstrate the utility of the new method with two existing physical model studies. By being consistent with the numerical framework, the internal method calculates the momentum terms with a much lower residual at computer precision, combined with greatly reduced calculation time and output storage requirements compared to post-processing techniques. The method developed here allows the accurate evaluation of the depth-integrated, mean momentum terms of wave-driven flows while taking advantage of the more complete representation of the wave dynamics offered by phase-resolving models. Furthermore, it provides an opportunity for advances in the understanding of nearshore processes particularly at more complex sites where wave nonlinearity and energy transfers are important.

1. Introduction

Wave-induced flows play an important role in driving nearshore processes along much of the world's coastline. In the nearshore zone, the transformation of waves results in forces that cause changes in mean water level (set-up and set-down) and mean currents. The mean currents that result from waves are the primary mechanism by which coastal sediments are transported, as well as other material such nutrients and contaminants. While wave orbital motions play a direct role in mobilizing sediment from the seabed, in many cases mean (wave or phase-averaged) currents advect suspended sediments and drive seasonal and longer term coastal changes. As a result, understanding the physical mechanisms driving mean currents is paramount to understanding a wide range of nearshore processes, which requires accurate calculations of the forces responsible for driving the mean flows.

The mean momentum equations, which have been derived by several authors (e.g., Mei et al., 2005; Svendsen, 2005), originate from

* Corresponding author at: School of Earth Sciences, The University of Western Australia, Crawley, WA 6009, Australia.
E-mail addresses: renan.silva@research.uwa.edu.au (R.F. da Silva), dirk.rijnsdorp@uwa.edu.au (D.P. Rijnsdorp), jeff.hansen@uwa.edu.au (J.E. Hansen), ryan.lowe@uwa.edu.au (R. Lowe), mbuckley@usgs.gov (M. Buckley), M.Zijlema@tudelft.nl (M. Zijlema).

https://doi.org/10.1016/j.ocemod.2021.101846
Received 29 January 2021; Received in revised form 2 June 2021; Accepted 9 July 2021
Available online 13 July 2021

time-averaging the Navier–Stokes equations over a time-scale much greater than an individual wave. By formally separating the wave forces (or radiation stress gradients) from the other terms, this provides a method to understand how waves drive water level gradients and nearshore currents. A number of studies have completed such analysis using field measurements (e.g., Feddersen et al., 1998; Feddersen and Guza, 2003; Apotsos et al., 2008; Hansen et al., 2014), laboratory experiments (e.g., Buckley et al., 2015; Haller et al., 2002; Stive and Wind, 1982) and numerical modelling (e.g., Long and Özkan Haller, 2005; Benedet and List, 2008; Hansen et al., 2013, 2015).

The momentum terms include spatial gradients in quantities derived from velocity and pressure profiles (see Section 2). A major limitation of field and laboratory measurements for doing this type of analysis arises from the fact that the measurement of the fine-scale spatial and temporal variability of velocities and pressure cannot be fully-resolved within surf zones even using the most advanced experimental techniques and extensive measurement arrays. In addition, velocity measurements close to the wave crest are difficult to perform in any setting. These challenges often result in the need to rely on linear wave theory (LWT) for the calculation of the radiation stress, which limits the accuracy of the calculation of their gradients. Alternatively, numerical models by their own nature solve momentum balances and as such allow for an accurate assessment of all momentum terms and a closure of the balance, namely, the sum of all momentum terms is on the order of computer precision as long as the calculation is consistent with the numerical approaches used in the model.

Two classes of wave modelling systems have been used to predict wave-driven flows, namely phase-averaged models (e.g., Delf3D-SWAN, Lesser et al., 2004) and phase-resolving models (e.g., SWASH, Zijlema et al., 2011). Phase-averaged models solve mean flow equations through coupling with wave-action models (e.g., SWAN, Booij et al., 1999), which calculate the time-averaged spatial and frequency propagation of wave energy. LWT expressions (Longuet-Higgins and Stewart, 1964) are used to calculate radiation stress gradients based on gradients in wave energy. These radiation stress gradients are then applied as an additional force in the flow model. In addition, phase-averaged models must rely on parameterization of physical processes that do not follow LWT (e.g., wave breaking, roller models). Therefore, phase-averaged models do not fully capture the radiation stress gradients but rely on LWT simplifications and parameterization to account for its effect on the mean flow. As phase-averaged models do not calculate the intra-wave flow, grid resolutions can be coarser than phase-resolving models allowing for larger time steps reducing the computational cost and allowing for the modelling of larger spatial and temporal scales.

Conversely, phase-resolving models, such as Computational Fluid Dynamics (CFD) type models (e.g., Chen et al., 1999; Dalrymple and Rogers, 2006; Wang et al., 2009; Lowe et al., 2019), non-hydrostatic (e.g., Zijlema et al., 2011; Ma et al., 2012), and Boussinesq type models (e.g., Kennedy et al., 2000; Nwogu, 1993), intrinsically account for the intra-wave motions (e.g., oscillatory velocities and pressures) that are responsible for mean flows. A key advantage of phase-resolving over phase-averaged models is their ability to resolve the nonlinear properties of waves propagating in the nearshore (e.g., nonlinear wave shape and energy transfers). Although phase-resolving models have been successfully validated to predict velocities and water levels, the focus of most studies has been on comparing wave parameters and wave-driven flow patterns (e.g., Peregrine, 1967; Berkhoff, 1972; Hirt and Nichols, 1981; Monaghan, 1994; Lin and Liu, 1998; Stelling and Zijlema, 2003; Feddersen et al., 2011; Ma et al., 2012; Buckley et al., 2014; Derakhti et al., 2016), with a lesser number of studies using the mean forces to investigate the mechanisms driving mean water levels and wave-driven flows (e.g., Rogers et al., 2013; Lowe et al., 2015, 2019; Sous et al., 2020).

To compute mean momentum balances, studies using phase-resolving models have conventionally used model output of velocity, pressure and water-level in a similar manner to how experimental observations would be analysed (albeit with higher spatial resolution). However, the estimation of the mean forces using the available model output does not necessarily guarantee that the momentum balance closes. The sum of all momentum terms, which should be zero (or at computer precision), is often the same order of magnitude as the net of the radiation stress gradient and pressure gradient which essentially drives the mean flow (e.g., Sous et al., 2020). Without a residual that is much less than the sum of the pressure and radiation stresses, or other likely important terms (e.g., bottom stress), the accurate assessment of the drivers of the flow can be compromised.

With advances in computational power, the use of phase-resolving models will expand and provide opportunities to understand nearshore processes, particularly at sites where wave non-linearity and energy transfers are important. To our knowledge, no phase-resolving model has the ability to output the depth-integrated mean momentum terms that ultimately drive nearshore mean water levels and currents. In this manuscript we present a new method to internally calculate the depth-integrated, mean momentum terms from the phase-resolving, non-hydrostatic numerical model SWASH (Zijlema et al., 2011; Zijlema and Stelling, 2008) consistent with a classical method to obtain the mean momentum balance (Mei et al., 2005). SWASH is an open-source code, and the methods developed here have been recently implemented in version 6.01, which is publicly available. This model has been extensively applied to calculate the transformation of surface waves in nearshore areas (e.g., Smit et al., 2014; Nicolae Lerma et al., 2017; Conde-Frias et al., 2017; Fiedler et al., 2018; Rooijen et al., 2020, to cite a few recent studies). Further, we demonstrate the improvements of this new method through its application to two existing physical model studies where an analysis of the momentum balance was conducted using the observed water levels and velocities (Haller et al., 2002; Buckley et al., 2015). While the methodology we develop can be applied at a wide range of sites we expect it to be particularly relevant for understanding the physical drivers of wave driven flows at sites with complex bathymetries. (e.g., with alongshore variable morphology) and locations where nonlinear wave processes are important and it is thus advantageous to use a phase-resolving wave-flow model.

2. Methodology

In this section, we outline the derivation of the depth-integrated, mean momentum terms from the governing equations, which allows for an interpretation of the forces that drive wave-driven mean water levels and currents in the nearshore. Next, we demonstrate how the same equations can be derived from the numerical framework of the SWASH model, allowing for an internal calculation of the mean momentum terms that is consistent with the classical method of Mei et al. (2005).

2.1. Governing equations

The Reynolds-Averaged Navier–Stokes (RANS) equations in the divergence form (or flux form, namely, with the momentum flux written with $\partial u_i u_j/\partial x_j$, rather than with $u_i \partial u_j/\partial x_j$), for an incompressible flow of constant density are (e.g., Anderson (1995),

$$\frac{\partial u_j}{\partial x_j} + \frac{\partial w}{\partial z} = 0, \tag{1}$$

$$\frac{\partial u_i}{\partial t} + \frac{\partial u_i u_j}{\partial x_j} + \frac{\partial u_i w}{\partial z} + \frac{\partial p}{\partial x_i} = \frac{\partial \tau_{ij}}{\partial x_j} + \frac{\partial \tau_{iz}}{\partial z}, \tag{2}$$

$$\frac{\partial w}{\partial t} + \frac{\partial w u_j}{\partial x_j} + \frac{\partial w w}{\partial z} + \frac{\partial p}{\partial z} = -g + \frac{\partial \tau_{zj}}{\partial x_j} + \frac{\partial \tau_{zz}}{\partial z}, \tag{3}$$

where x_i and z denote horizontal ($i = 1,2$) and vertical directions, u_i (x_i, z, t) and w (x_i, z, t) are the horizontal and vertical velocities, t is time, p (x_i, z, t) is the total pressure normalized by the reference density ρ, and τ_{ij} (x_j, z, t) are the Reynolds (turbulent) stresses (see summary of notation in Table 1).

Table 1
Notation.

Symbol	Definition	Unit
d	Still water depth	m
g	Gravity acceleration	m s^{-2}
h	Total water depth	m
H_0	Deep water wave height	m
H	Wave height	m
H_{rms}	Rms wave height	m
$H_{rms,0}$	Deep water rms wave height	m
k_w	Wave number	rad m^{-1}
L_0	Deep water wavelength	m
$L_{B,P}$	Peak wavelength at breaking position	m
p	Total pressure (normalized by density)	m^2 s^{-2}
q	Non-hydrostatic pressure (normalized by density)	m^2 s^{-2}
S_{ij}	Radiation stress (normalized by density)	m^3 s^{-2}
t	Time	s
T	Wave period	s
T_P	Peak wave period	s
u_i	Instantaneous horizontal velocity	m s^{-1}
$\widetilde{u}_i$	Oscillatory horizontal velocity—calculated by subtracting U from u, see Eq. (8)	m s^{-1}
u_{lf}	Oscillatory horizontal velocity—calculated by subtracting U_{lf} from u, see Eq. (19)	m s^{-1}
U	Mass-flux velocity	m s^{-1}
U_d	Instantaneous depth-averaged velocity	m s^{-1}
U_E	Eulerian (or depth-averaged, mean) velocity	m s^{-1}
U_{lf}	Low-frequency mass-flux velocity	m s^{-1}
w	Instantaneous vertical velocity	m s^{-1}
x_i	Horizontal position	m
z	Vertical position	m
β	Reef slope	–
ζ	Water level deviation from d	m
ζ_{lf}	Low-frequency water level deviation from d	m
ξ_0	Irribarren parameter	–
ϕ	Mass flux	m^2 s^{-1}
τ_{ij}	Reynolds (turbulent) stress normalized by density	m^2 s^{-2}
ω	Relative vertical velocity	m s^{-1}

The kinematic boundary conditions at the bottom and at the free-surface are

$$w_\zeta = \frac{\partial \zeta}{\partial t} + u_{j,\zeta}\frac{\partial \zeta}{\partial x_j}, \tag{4}$$

$$w_{-d} = -u_{j,-d}\frac{\partial d}{\partial x_j}, \tag{5}$$

where ζ (x_i,t) is the water level and d (x_i) is the still water depth. With the depth-integration of the continuity equation, Eq. (1), and by using the kinematic boundary conditions, Eqs. (4) and (5), the global continuity equation is obtained as follows,

$$\frac{\partial \zeta}{\partial t} + \frac{\partial \int_{-d}^{\zeta} u_j dz}{\partial x_j} = 0. \tag{6}$$

Consistent with the numerical implementation within SWASH, for the application of the dynamic boundary conditions we assume that the viscous stresses are zero, the atmospheric pressure is constant and null at the free surface, and wind is absent and thus there is no tangential stress on the surface. Furthermore, bottom friction is included through imposing a tangential stress at the seabed.

2.2. The depth-integrated, phase-averaged momentum balance—theory

Several versions of the depth-integrated, wave-flow equations exist in the literature, (e.g., Mei et al., 2005—Eq. 11.2.24; Svendsen, 2005—Eq. 11.5.11). Although they always start with the Navier–Stokes equations, the methodology for decomposing the velocities and separating the radiation stress gradients (see below) may differ, resulting in different interpretations of momentum terms. In this work, we opted to use an interpretation similar to Mei et al. (2005) given its extensive usage. The essential step to obtain Mei et al.'s (2005) depth-integrated, mean flow equations is to decompose the velocity signal into a slowly varying component ($U(x_i)$, associated with the mean flow and hereafter referred to as the mass-flux velocity) and a fluctuating component ($\tilde{u}(x_i,z,t)$, primarily associated with the waves),

$$U_i = \frac{\left\langle \int_{-d}^{\zeta} u_i dz \right\rangle}{d + \langle \zeta \rangle}, \tag{7}$$

$$\widetilde{u}_i = u_i - U_i, \tag{8}$$

where $\langle\,\rangle$ indicates averaging over many wave periods. Apart from the waves, the fluctuating component contains contributions due to vertical variations in the mean velocity profile. For coastal applications, in which gravity waves are the main interest, the oscillatory velocity $\widetilde{u}_i$ is predominantly due to waves.

Substituting the flow contributions, Eqs. (7) and (8) into the RANS equations, Eqs. (1) and (2), and integrating over the total water depth and averaging over many wave periods results in the depth-integrated, mean momentum equation (see Appendix A for details),

$$\overbrace{\left\langle \frac{\partial \int_{-d}^{\zeta} \widetilde{u}_i dz}{\partial t} \right\rangle}^{local\ acceleration} + \overbrace{(d + \langle \zeta \rangle) U_j \frac{\partial U_i}{\partial x_j}}^{advective\ acceleration} + \overbrace{g(d + \langle \zeta \rangle)\frac{\partial \langle \zeta \rangle}{\partial x_i}}^{pressure\ gradient} + \overbrace{\frac{\partial S_{ij}}{\partial x_j}}^{radiation\ stress\ gradient} - \overbrace{\langle q_{-d} \rangle \frac{\partial d}{\partial x_i}}^{hydrodynamic\ reaction\ at\ bottom} - \overbrace{\frac{\partial \left\langle \int_{-d}^{\zeta} \tau_{ij} dz \right\rangle}{\partial x_j}}^{Reynolds\ stress\ horizontal gradient} + \overbrace{\langle \tau_{-d,iz} \rangle}^{bottom\ friction} = 0, \tag{9}$$

in which q (x_j,z,t) is the non-hydrostatic pressure ($q = p - g(z + \zeta)$), whose mean value at the bottom equals the dynamic pressure. The excess momentum flux due to the presence of waves or radiation stress (Longuet-Higgins and Stewart, 1964), S_{ij}, is given as,

$$S_{ij} = S_{orb,ij} + S_{pres} = \overbrace{\left\langle \int_{-d}^{\zeta} \widetilde{u}_i \widetilde{u}_j dz \right\rangle}^{S_{orb,ij}} + \overbrace{\left\langle \int_{-d}^{\zeta} p dz \right\rangle}^{S_{pres}} - 0.5\, g (d + \langle \zeta \rangle)^2, \tag{10}$$

where the subscripts *orb* and *pres* indicate the contributions for the wave orbital flow and pressure, respectively. As our derivation begins with the RANS equations, the excess momentum flux S_{ij} (Eq. (10)), does not contain any contribution from turbulent velocities and can be identified as the radiation stress. This is a slight deviation from the definition used by Mei et al. (2005), where S_{ij} includes turbulent velocities and is thus not strictly the radiation stress due to the waves.

Our derivation assumes a stationary mass flux velocity (i.e., $\partial U_i/\partial t = 0$), as the time scale with which sea states change is large compared to the short wave time scale. This is consistent with most field and laboratory studies, and numerical phase-resolving modelling approaches, which consider a single sea-state during which the wave and water level boundary conditions are quasi-stationary. From this assumption, we obtain a mean local acceleration that depends only on oscillatory velocities ($\widetilde{u}_i$), whereas Mei et al.'s (2005) derivation also includes an unsteady U_i, that results in a local acceleration as a function of its time derivative $\left((d + \langle \zeta \rangle)\frac{\partial U_i}{\partial t}\right)$.

An advantage of using the depth-integrated, mean momentum equation in a format analogous to Mei et al. (2005) is the adoption of mass flux velocities (U_i), since unlike Eulerian velocities ($U_E = \left\langle \int_{-d}^{\zeta} u_i dz/(d + \zeta) \right\rangle$), the mass flux velocities contain information on the total mean mass transport by the waves. This method is analogous to the Generalized Lagrangian Mean (GLM) approach (Andrews and Mcintyre, 1978) used in phase-averaged coupled wave-circulation models (e.g., Lesser et al., 2004).

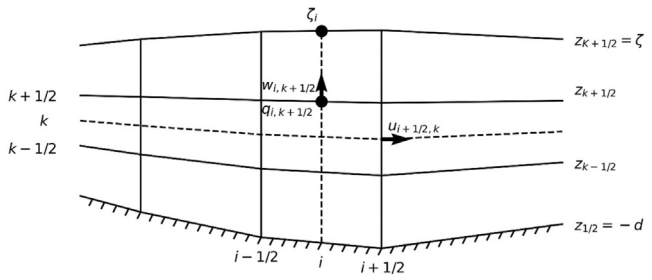

Fig. 1. Staggered grid arrangement of unknowns and vertical grid definition with layer interfaces of SWASH multi-layer model.

2.3. Numerical implementation within SWASH

Here we present the method to calculate the depth-integrated, mean momentum terms within the phase-resolving non-hydrostatic model SWASH. SWASH is a numerical implementation of the governing equations, Eqs. (1)–(3). The model can be used in 1D, 2DH (cross and alongshore dimensions with one vertical layer), 2DV (cross-shore and vertical dimensions) as well as fully 3D. We implemented the method to extract the depth-integrated, mean momentum balance for all available modes. Here, we only show the implementation for SWASH 2DV to keep the paper brief and concise as the methodology is the same for all other modes and the extension to 3D is straightforward and does not introduce any new concepts.

2.3.1. SWASH governing equations

In SWASH multi-layer mode, a boundary-fitted grid is used in the vertical direction, with the domain being divided into K layers (see Fig. 1). Each layer is positioned between the interfaces given by $z_{k+1/2}(x,t)$ with $k = 0,1,\ldots,K$, in such a way that each layer has a thickness h_k defined as $z_{k+1/2} - z_{k-1/2} = f_k h$, where $h(x,t)$ is the total depth ($h = z_{K+1/2} - z_{1/2} = d + \zeta$) and with $0 \le f_k \le 1$ and $\sum_k f_k = 1$, with f_k being the fraction of the instantaneous depth. Variables are arranged in a staggered arrangement, and all equations are integrated over each layer to obtain a set of layer-averaged equations that are solved in SWASH (Zijlema and Stelling, 2008)—see Fig. 1 and Appendix B.3 for more details.

The starting point of the derivation of the mean momentum terms is consideration of the horizontal momentum equation in the form that is implemented in SWASH. In the multi-layer framework of SWASH, the layer-averaged momentum equation is implemented in its non-flux or advective form,

$$\begin{aligned}\frac{\partial u_k}{\partial t} &+ \frac{1}{h_k}\left(\frac{\partial \phi_k u_k}{\partial x} - u_k\frac{\partial \phi_k}{\partial x}\right)\\ &+ \frac{1}{h_k}\left(\overline{u}^z_{k+1/2}\omega_{k+1/2} - \overline{u}^z_{k-1/2}\omega_{k-1/2} - u_k\omega_{k+1/2}\right.\\ &\left.+u_k\omega_{k-1/2}\right) + g\frac{\partial \zeta}{\partial x} + \frac{1}{h_k}\frac{\partial h_k \overline{q}^z_k}{\partial x} - \frac{q_{k+1/2}}{h_k}\frac{\partial z_{k+1/2}}{\partial x}\\ &+ \frac{q_{k-1/2}}{h_k}\frac{\partial z_{k-1/2}}{\partial x} = 0,\end{aligned} \tag{11}$$

where the mass flux ϕ_k is defined as $h_k u_k$ and the relative vertical velocity is given as $\omega_{k+1/2} = w_{k+1/2} - \frac{\partial z_{k+1/2}}{\partial t} - \frac{\overline{u}^z_{k+1/2}\partial z_{k+1/2}}{\partial x}$. Note that Eq. (11) can still be made momentum conservative at the discrete level (for details, see Zijlema, 2019). With the staggered variable arrangement, the vertical velocities w and the non-hydrostatic pressures q are defined at the cell corners ($z_{k+1/2}$), whereas the horizontal velocities u are defined at the cell centres (z_k), see Fig. 1. The overbars with superscripts z denote a linear interpolation of the variable from its surrounding neighbours (see Zijlema and Stelling (2008) for more details).

2.3.2. The depth-integrated, phase-averaged momentum balance—SWASH

In order to calculate the depth-integrated, mean momentum terms from SWASH, we related each term in Eq. (11) to its equivalent term in the depth-integrated, mean momentum equation, Eq. (9) (for details of this derivation, see Appendices B.1 and B.2). To achieve this, we first derived the layer-integrated momentum equation in the flux form that is analogous to the depth-integrated momentum equation in divergence form, Eq. (A.1), used for deriving Eq. (9). The integration by vertical layers of the horizontal momentum equation, Eq. (2), in the flux form – neglecting for simplicity the Reynolds stress gradients – is done as follows,

$$\int_{z_{k-1/2}}^{z_{k+1/2}}\frac{\partial u}{\partial t}dz + \int_{z_{k-1/2}}^{z_{k+1/2}}\frac{\partial uu}{\partial x}dz + \int_{z_{k-1/2}}^{z_{k+1/2}}\frac{\partial wu}{\partial z}dz + \int_{z_{k-1/2}}^{z_{k+1/2}}\frac{\partial p}{\partial x}dz = 0. \tag{12}$$

After reworking each individual term, we obtain the layer-integrated momentum equation in the flux form,

$$\begin{aligned}u_k\frac{\partial h_k}{\partial t} &+ h_k\frac{\partial u_k}{\partial t} + \frac{\partial \phi_k u_k}{\partial x} + \overline{u}^z_{k+1/2}\omega_{k+1/2} - \overline{u}^z_{k-1/2}\omega_{k-1/2} + gh_k\frac{\partial \zeta}{\partial x}\\ &+\frac{\partial h_k \overline{q}^z_k}{\partial x} - q_{k+1/2}\frac{\partial z_{k+1/2}}{\partial x} + q_{k-1/2}\frac{\partial z_{k-1/2}}{\partial x} = 0.\end{aligned} \tag{13}$$

Unlike the SWASH horizontal momentum equation, Eq. (11), the depth integration of Eq. (13) allows the prompt identification of each equivalent term in Eq. (A.1), thus it can be converted to Eq. (9) following the steps described in Appendix A. Therefore, we need to convert the SWASH horizontal momentum equation, Eq. (11), which is written in the advective form, to the divergence form (i.e., to reach Eq. (13)). To accomplish this, we derived the layer-integrated continuity equation that is obtained through the integration of the local continuity equation over the vertical,

$$\begin{aligned}\int_{z_{k-1/2}}^{z_{k+1/2}}\frac{\partial u}{\partial x}dz &+ \int_{z_{k-1/2}}^{z_{k+1/2}}\frac{\partial w}{\partial z}dz\\ &= \frac{\partial \int_{z_{k-1/2}}^{z_{k+1/2}} u dz}{\partial x} - \overline{u}^z_{k+1/2}\frac{\partial z_{k+1/2}}{\partial x} + \overline{u}^z_{k-1/2}\frac{\partial z_{k-1/2}}{\partial x}\\ &+w_{k+1/2} - w_{k-1/2} = 0.\end{aligned} \tag{14}$$

The layer-integrated continuity equation, Eq. (14), can be rewritten using the local mass flux ϕ and the relative vertical velocity ω as follows,

$$\frac{\partial h_k}{\partial t} + \frac{\partial \phi_k}{\partial x} + \omega_{k+1/2} - \omega_{k-1/2} = 0. \tag{15}$$

To reach Eq. (13) from Eq. (11), we first multiply Eq. (11) by the layer thickness h_k, and then add the product of the local continuity equation (Eq. (15)), and the layer-averaged velocity u_k. In our method, the computation of the instantaneous momentum terms of Eq. (13) takes into account the numerical discretization of all momentum terms (see Appendix B.3), ensuring that the instantaneous residual is on the order of machine precision (see Section 3.3.1).

To obtain the SWASH instantaneous depth-integrated momentum equation (i.e., an equivalent form of Eq. (A.1)), we integrate Eq. (13) in the vertical through the sum of the layer-integrated momentum terms as follows,

$$\begin{aligned}\sum_{k=1}^{k=K}\left[u_k\frac{\partial h_k}{\partial t} + h_k\frac{\partial u_k}{\partial t}\right] &+ \sum_{k=1}^{k=K}\frac{\partial \phi_k u_k}{\partial x}\\ &+ \sum_{k=1}^{k=K}\left[gh_k\frac{\partial \zeta}{\partial x} + \frac{\partial h_k \overline{q}^z_{k+1/2}}{\partial x}\right] - q_{-d}\frac{\partial d}{\partial x} = 0,\end{aligned} \tag{16}$$

where this depth-integration results in the cancelling of some terms (e.g., $\sum_{k=1}^{k=K}\left[\overline{u}^z_{k+1/2}\omega_{k+1/2} - \overline{u}^z_{k-1/2}\omega_{k-1/2}\right] = 0$). The term-by-term comparison of the SWASH depth-integrated momentum equation, Eq. (16), with the depth-integrated momentum equation (Eq. (A.1)) is presented in Table 2.

With the time averaging of Eq. (16) over many wave periods and separating the wave and mean flow components (see Appendix A), we can finally calculate each equivalent term of Eq. (9) within the SWASH numerical framework (see Table 3).

Table 2
Comparison between each term of the SWASH depth-integrated momentum equation, Eq. (16), and the original depth-integrated momentum equation, Eq. (A.1).

Term from the depth-integrated momentum Equation, Eq. (A.1)	Term from the SWASH depth-integrated momentum equation, Eq. (16)	Physical description
$\frac{\partial \int_{-d}^{\zeta} u\, dz}{\partial t}$	$\sum_{k=1}^{k=K}\left[u_k \frac{\partial h_k}{\partial t} + h_k \frac{\partial u_k}{\partial t}\right]$	Local acceleration
$\frac{\partial \int_{-d}^{\zeta} uu\, dz}{\partial x}$	$\sum_{k=1}^{k=K} \frac{\partial \phi_k u_k}{\partial x}$	Advective acceleration
$\int_{-d}^{\zeta} \frac{\partial p}{\partial x} dz$	$\sum_{k=1}^{k=K}\left[g h_k \frac{\partial \zeta}{\partial x} + \frac{\partial h_k \overline{q}_k^z}{\partial x}\right] - q_{-d} \frac{\partial d}{\partial x}$	Total pressure gradient

2.3.3. Implementation of the method

To calculate the depth-integrated, mean momentum terms within SWASH, the instantaneous depth-integrated momentum terms (see Table 2), along with a few other instantaneous variables (e.g., the global mass flux $\sum_{k=1}^{k=K} u_k h_k$, the water level ζ, the water depth h and the variation in time of the water level $\frac{\partial \zeta}{\partial t}$ (or instantaneous water depth $\frac{\partial h}{\partial t}$)), are stored at every model time step after spin-up (see below). At the end of the simulation, their time-average is computed. These time-averaged (total) advective and pressure terms (i.e., the time-average of the terms in Table 2) contain contributions from both the waves and mean flow. To separate their contributions, and to extract the radiation stress gradient, we firstly compute the mean-flow terms of the mean-momentum equation, Eq. (9) (e.g., the advective acceleration and pressure gradient) using a simple finite difference scheme (with central differences for the spatial derivatives). Subsequently, we compute the remaining terms (e.g., local acceleration and radiation stress gradient) by subtracting the mean flow contributions from the time-averaged (total) advective and pressure terms (Table 3). In this manner, we recast the depth-integrated terms from SWASH into a form that is consistent with the notation of the mean momentum equation (Eq. (9)).

In SWASH 6.01, where this new method has been implemented, the user can output all depth-integrated, mean momentum terms from Eq. (9) in a similar way to how mean quantities (e.g., set-up and significant wave height) are currently output, namely by defining the averaging time (i.e., after spin-up time).

The primary evaluation of our method was to ensure that the internal momentum balance closes, which was done by calculating the residual of all momentum terms. We verified that this residual was at the same level as the computational numerical precision [O (10^{-8} m^2 s^{-2}) for variables with 32 bits] (see Section 3.3.1). In addition, we ensure that the implementation of the method has a negligible effect on the overall speed of SWASH simulations (see Section 4) given the low memory allocation needed.

3. Applications

The utility of the SWASH source code modifications described above is demonstrated using two laboratory datasets in which corresponding papers discuss mean momentum balances derived from instrument measurements in 2D and 3D: irregular waves over a steeply sloping fringing reef in a 2D wave flume (Buckley et al., 2015), and regular waves over barred beaches with rip channels in a 3D wave basin (Haller et al., 2002). For both cases, extensive water level and velocity measurements were made, and we validate the modelled mean flow properties using the observations. Next, we determine the physical mechanisms that characterize the mean flow through the analysis of the momentum terms using the method developed here. Further, we demonstrate the accuracy of the new internal method by calculating the momentum balance residuals and comparing these to the residuals obtained through a post-processing approach.

3.1. Irregular waves over steeply sloping reef

3.1.1. Description of experiment and SWASH setup

The focus of the Buckley et al. (2015) study was to investigate the mean momentum dynamics through the surf zone of a steep fringing reef profile. The experiments were conducted in the 55-m-long wave flume where a reef profile was constructed with a 1:5 fore reef slope, followed by a horizontal 14 m reef flat and a 1:12 beach (Buckley et al., 2015, and Fig. 2). Irregular waves were generated with a piston-type wave maker with second-order wave generation and active reflection

Table 3
Method to calculate terms from the depth-integrated, mean momentum equation, Eq. (9), with the SWASH depth-integrated momentum equation, Eq. (16).

Term from the depth-integrated, mean momentum equation, Eq. (9)	Term from the SWASH depth-integrated momentum equation, Eq. (16).	Physical description
U	$\frac{\left\langle \sum_{k=1}^{k=K} u_k h_k \right\rangle}{(d + \langle\zeta\rangle)}$	Mass flux velocity
$\left\langle \frac{\partial \int_{-d}^{\zeta} \tilde{u} dz}{\partial t} \right\rangle$	$\left\langle \sum_{k=1}^{k=K}\left[u_k \frac{\partial h_k}{\partial t} + h_k \frac{\partial u_k}{\partial t}\right]\right\rangle - U \left\langle \frac{\partial (d+\zeta)}{\partial t} \right\rangle$	Local acceleration[a]
$(d + \langle\zeta\rangle) U \frac{\partial U}{\partial x}$	$(d + \langle\zeta\rangle) U \frac{\partial U}{\partial x}$	Advective acceleration
$g(\langle\zeta\rangle + d) \frac{\partial \langle\zeta\rangle}{\partial x}$	$g(d + \langle\zeta\rangle) \frac{\partial \langle\zeta\rangle}{\partial x}$	Pressure gradient
$\frac{\partial S_{xx_{orb}}}{\partial x}$	$\left\langle \sum_{k=1}^{k=K} \frac{\partial \phi_k u_k}{\partial x} \right\rangle - (d + \langle\zeta\rangle) U \frac{\partial U}{\partial x} + U \left\langle \frac{\partial (d+\zeta)}{\partial t} \right\rangle$	Radiation stress gradient – orbital velocities[b]
$\frac{\partial S_{xx_{pres}}}{\partial x}$	$\left\langle \sum_{k=1}^{k=K}\left[g h_k \frac{\partial \zeta}{\partial x} + \frac{\partial h_k \overline{q}_{k+\frac{1}{2}}^z}{\partial x}\right]\right\rangle - g(\langle\zeta\rangle + d) \frac{\partial \langle\zeta\rangle}{\partial x}$	Radiation stress gradient – pressure[c]
$-\langle q_{-d}\rangle \frac{\partial d}{\partial x}$	$-\langle q_{-d}\rangle \frac{\partial d}{\partial x}$	Hydrodynamic reaction at bottom

[a]See Eq. (A.6) and Table 2.
[b]See Eq. (A.7) and Table 2.
[c]See Eq. (A.11) and Table 2.

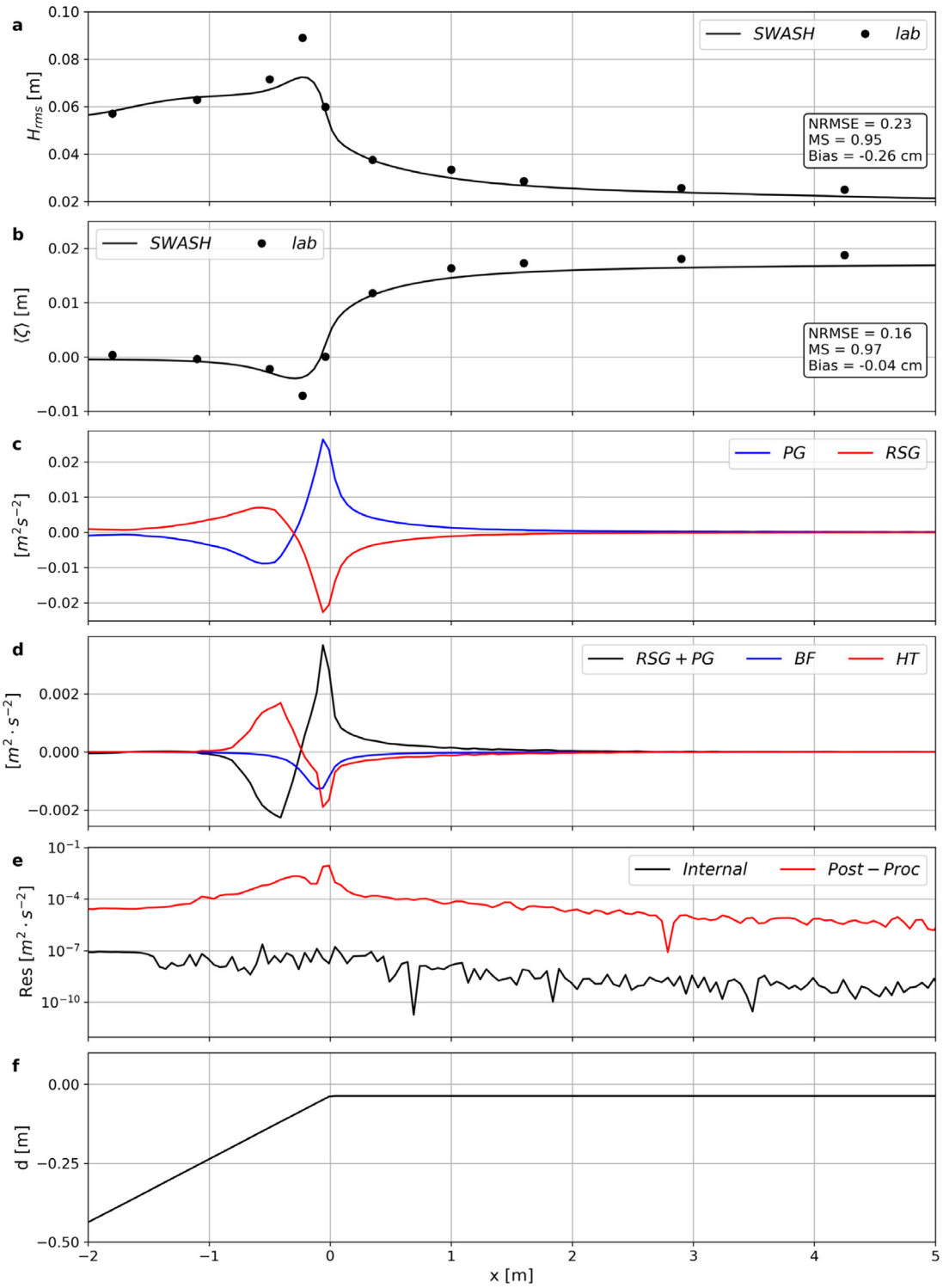

Fig. 2. Cross-shore variation (x) in waves propagating over sloping reef (Buckley et al., 2015): (a) root mean square wave height H_{rms}. (b) Mean water level $\langle\zeta\rangle$ (c) Radiation stress gradient (RSG) and pressure gradient (PG). (d) Reynolds stress horizontal gradients (HT), bottom friction (BF) and mismatch between radiation stress gradient and pressure gradient (*RSG* + *PG*), one order of magnitude lower than *RSG* and *PG* shown in subplot (c). The remaining terms – local and advective acceleration – are negligible. (e) Residual with internal and post-processing method. (f) Depth profile. Measurement (circles) and SWASH run (solid line). Note the change in vertical axis scales in panels (c), (d), and (e). *NRMSE* refers to the root mean square error normalized by the standard deviation, and *MS* is the Murphy Skill (Murphy, 1988).

compensation. A set of 17 resistance wave gauges were used to measure water levels at 40 Hz, with a higher density of measurements in the surf zone region (Fig. 2). Here we analyse data from 'Run 2', with the following experimental conditions: $H_{rms,0} = 0.06$ m and $T_p = 2.3$ s (or in field scale, $H_{rms,0} = 2.2$ m and $T_p = 13.6$ s), where $H_{rms,0}$ is the root-mean square deep water wave height and T_p is the peak wave period. This run lasted for 42 min, and waves were in the plunging regime, as calculated by the Irribarren parameter ($\xi_0 = \frac{\beta}{\sqrt{\frac{H_{rms,0}}{L_0}}} = 2.4$, where β is the reef slope and L_0 is the deep water wavelength).

SWASH was applied to reproduce 'Run 2' in Buckley et al. (2015) with a uniform horizontal grid size of 0.05 m, an initial time step

of 0.005 s and two vertical layers, which are sufficient for resolving the wave dispersion (Zijlema et al., 2011) following the analysis of the normalized water depth $k_w d$, in which k_w is the wave number. A Fourier-type boundary condition was prescribed at the wave maker, with the Fourier components calculated with the incident wave signal - separated with a linear frequency domain algorithm (e.g., Buckley et al., 2015) - of measured water levels at the seaward most gauge. In SWASH, these components are internally converted into a velocity time series using LWT expressions. A spin-up period of 12 min was applied corresponding to about 287 waves. All mean output variables including the momentum terms were calculated at each grid cell over the remaining 30 min of the simulation, or about 782 waves, consistent with the analysis of the laboratory observations (Buckley et al., 2015).

3.1.2. Model performance

To quantify the overall model accuracy, we calculated three performance indicators for the wave heights and mean water levels, the root mean square error normalized by the standard deviation (NRMSE), the Murphy Skill (MS, defined below), and the bias. Murphy Skill (Murphy, 1988) is defined by:

$$MS = 1 - \sum_{i}^{N} \left(y^i_{mod} - y^i_{obs}\right)^2 / \sum_{i}^{N} \left(y^i_{obs} - \overline{y_{obs}}\right)^2, \tag{17}$$

where y^i_{mod} and y^i_{obs} are the modelled and observed variables of interest and $\overline{y_{obs}}$ corresponds to the average of the observed variables over N samples. MS was calculated to quantify the model performance, with values $MS < 0.5$, $0.5 < MS < 0.75$ and $MS > 0.75$ representing poor, moderate and high prediction scores, respectively. Lower values of NRMSE and bias indicate better performance.

The analysis of the performance indicators shows that the model results accurately reproduce the observations for both wave height (Fig. 2a) and mean water level (Fig. 2b). The wave heights are slightly overestimated by SWASH in the shoaling zone, except for the measured maximum wave height near the breaking point, which is underestimated by the model, and in the surf zone the model agreement is excellent. The modelled mean water levels are similar to measurements in the shoaling zone, except for the measured minimum set-down, which is underestimated, and in the surf zone they are slightly underestimated. The good performance in the calculation of the wave parameters gives us confidence that SWASH provides a robust representation of the dominant surf zone hydrodynamic processes.

3.1.3. Momentum balance analysis

In both the observations and SWASH predictions, the waves shoal on the slope, with wave heights increasing up to 30% followed by breaking on the reef crest and more gradual dissipation on the reef approaching the beach (Fig. 2a). Wave shoaling results in set-down followed by set-up as waves break near the reef crest (Fig. 2b). As expected for this 2D (closed) flume case, the depth-averaged mass flux velocities are negligible everywhere in the reef profile (not shown).

The momentum balance analysis indicates that the dominant forces are the radiation stress gradient (RSG) and pressure gradient (PG, Fig. 2c). The wave shoaling and set-down correspond to a positive and negative radiation stress gradient and pressure gradient, respectively. This pattern is reversed in the surf zone, consistent with wave breaking and set-up generation. The maximum absolute forces occur at the break point, and the pressure gradient and radiation stress gradient are in near balance across the entire profile. Their net is balanced by the sum of the bottom friction (BF) and Reynolds stress horizontal gradients (HT, Fig. 2d, note order of magnitude difference in scales from Fig. 2c). The bottom friction term (BF) is always negative, consistent with a persistent undertow. The Reynolds stress horizontal gradient term is introduced to prevent spurious motions when the hydrostatic front approximation is activated in the breaking zone (Smit et al., 2013). These results are conceptually in agreement with the findings from Buckley et al. (2015), however, we do not try and make a direct comparison with their momentum terms due to the inconsistencies between the calculation methods (e.g., for the calculation of the radiation stresses, Buckley et al. (2015) needed to use LWT and a parameterization of the wave roller to reproduce the observed wave set-up).

3.2. Wave-driven flow on a barred beach with rip channels

3.2.1. Description of experiment and SWASH setup

The experimental investigation of Haller et al. (2002) consists of a comprehensive laboratory study on rip currents over an alongshore heterogeneous coast with non-zero cross-shore mass fluxes. The experiments were carried out in a rectangular directional wave basin at the University of Delaware (length 17.2 m, width 18.2 m) with a flap type wavemaker with 34 paddles. The bottom profile was constructed to have a 1:5 slope in the region 1.5 to 3 m from the wavemaker, followed by a 1:30 slope in the remaining 15 m of the basin. A barred beach with two rip channel was superimposed on an otherwise alongshore uniform shoreface (Fig. 3 and Haller et al., 2002).

Here we study the data from 'Test B', which encompasses the most extensive measurements by Haller et al. (2002). This test consisted of monochromatic shore-normal waves with deep water wave height H_0 of 0.05 m and wave period T of 1 s (or in field scale H_0 of 2.5 m and T of 7 s assuming a length scale ratio of 1:50) propagating over an alongshore heterogeneous shoreface that resulted in bar/rip channel circulation cells. Ten capacitance wave gauges (Fig. 3a,b) and three side-looking acoustic Doppler velocimeter (ADVs, Fig. 3c) were used to measure time series of water levels and velocities, respectively, both with a frequency of 10 Hz. Forty repetitions of 'Test B' were conducted with different spatial configurations thus allowing over 100 observation points throughout the laboratory basin. Each test lasted for 27 min and 18.4 s (or 1638 waves).

We reproduced 'Test B' in SWASH 3D with a uniform horizontal grid size of 0.05 m, an initial time step of 0.01 s and with two vertical layers, found to be sufficient after analysis of the normalized water depth kd, as discussed in Section 3.1.1. We imposed monochromatic shore-normal waves on the offshore boundary, and lateral sidewalls were modelled as fully reflective boundaries. The Reynolds stresses are calculated with the eddy viscosity closure model following Smagorinsky (1963) for the horizontal direction.

We analyse the results after a spin-up period of 102.4 s, or 102 wave periods, in a similar way as Haller et al. (2002). All mean output variables including the momentum terms were calculated at each grid cell for the remaining 1536 s of the simulation, or 1536 wave periods.

3.2.2. Model performance

We conducted a statistical analysis similar to the previous example (Section 3.1.2) to examine the model's performance. The model performance indicators demonstrate the model is reproducing both the wave heights (Fig. 3d) and mean water levels (Fig. 3e). In addition, the comparison between calculated and observed normalized wave heights and mean water levels (Fig. 3a,b, respectively, where the coloured circles represent the measurements) show similar patterns and an overall satisfactory model performance.

The experimental velocity measurements were conducted with ADVs (Haller et al., 2002), thus only a single point in the vertical was available. As we applied SWASH with two vertical layers (Section 3.2.1), the model does not compute the velocities at the same vertical position. For simplicity, we qualitatively compared the depth-averaged Eulerian velocities ($U_E = \left\langle \int_{-d}^{\zeta} u_i dz/(d+\zeta) \right\rangle$) from SWASH with the Eulerian ADV velocities ($u_E = \langle u \rangle$) (Fig. 3c). The comparison between the velocities from model and observations (Fig. 3c) shows overall similar flow patterns and magnitude.

The agreement between model and observations indicates the model does an overall good job in reproducing the wave heights (Fig. 3a,d), mean water level (Fig. 3b,e) and mean currents (Fig. 3c), allowing us to assess the contributions of the mean momentum terms to the mean water levels and currents.

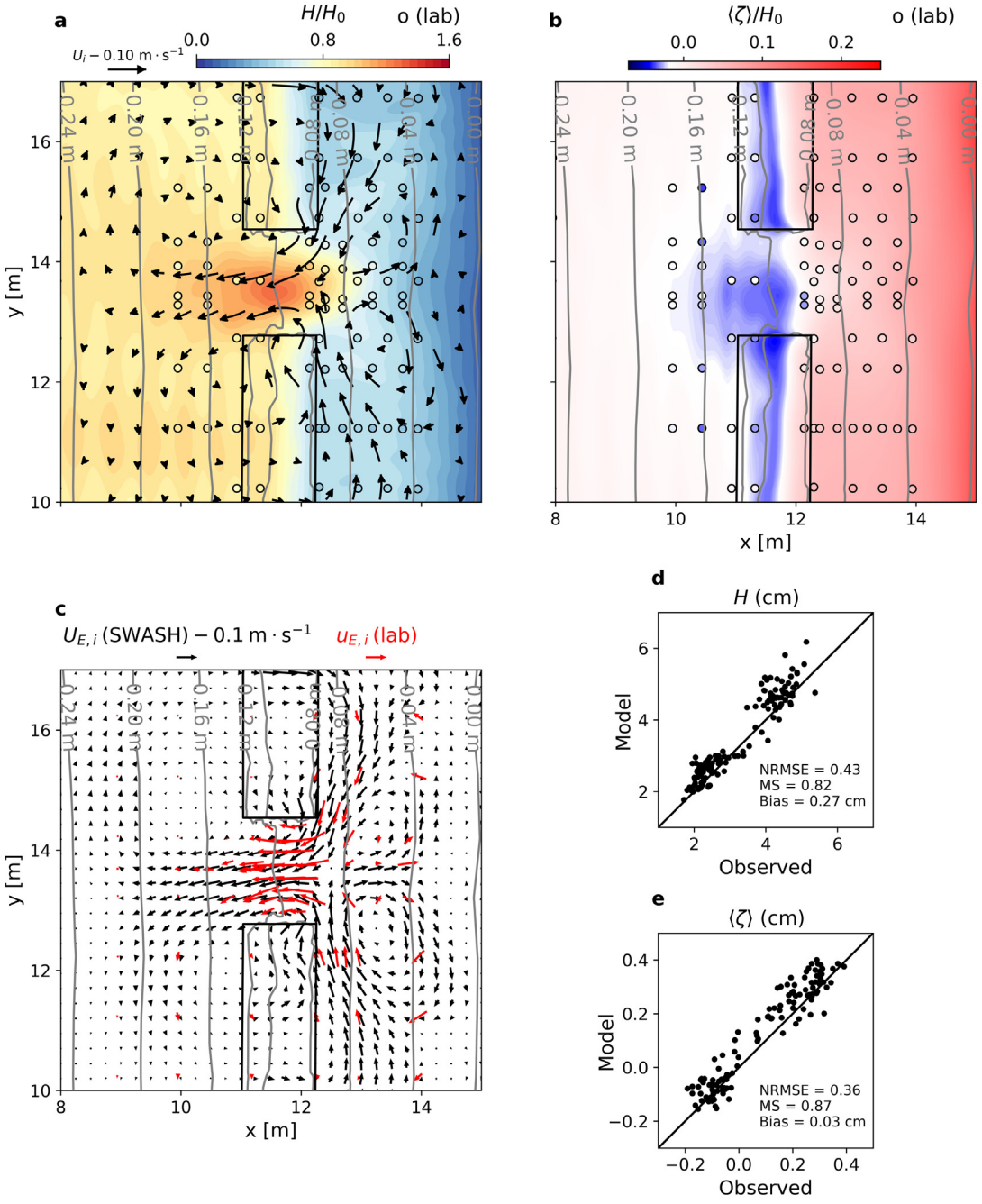

Fig. 3. Map view (a–c) and validation (d–e) of wave parameters and flow pattern of barred beach with rip channels (Haller et al., 2002); only showing a portion of the wave basin focusing on one of the rip channels for visual clarity): (a) normalized wave height H/H_0 (colours), with coloured circles representing the measurements (or lab) and mass-flux velocity U_i (streamlines represented by the arrows.) (b) Normalized mean water level $\langle\zeta\rangle/H_0$ (colours), with coloured scatters giving the measurements and mass-flux velocity U_i (arrows). (c) Eulerian velocities U_E. (d) Wave height H prediction versus observation. (e) Mean water level $\langle\zeta\rangle$ prediction versus observation. Solid grey lines represent the depth contours, and the solid black lines give the position of the bars. *NRMSE* refers to the root mean square error normalized by the standard deviation, and *MS* is the Murphy Skill (Murphy, 1988).

3.2.3. Mechanics of the wave-driven flow

The shore-normal waves gradually shoal as they propagate up the slope. Once the waves reach the bar they break while the waves in the rip channel further increase in height due to the opposing current (Fig. 3a,c). A moderate set-down (Fig. 3b) is observed at the lower shoreface, which persists near the bar-system. Over the bars, the wave breaking results in a sharp increase in the mean water level (e.g., set-up) that remains constant up to the second breaking location near the shore where the set-up increases again. Through the rip channels, the mean water levels progressively increase towards the shoreline.

The mass flux velocities (Fig. 3a) are dominated by a 4-cell circulation pattern. The first cell ($11 < x < 13$ m; $10 < y < 12.5$ m) is defined by the moderate onshore flow over the bars, which stems from the wave-breaking. Shoreward of the bar, this flow diverges and feeds alongshore currents towards the rip channels. The second cell ($11 < x < 13$ m; $12.5 < x < 14.5$ m) is characterized by the convergence of the flow coming from the bars and by the strong offshore flow over the rips. The mean discharge over the rips and the bars is about the same (± 0.03 m^{3}s^{-1}), consistent with a closed circulation cell. The third cell ($13 < x < 15$ m; $12.5 < y < 14.5$ m) occurs in the lee of the rip channels, where waters flow shoreward, due to the wave breaking, and diverges away from the coastline. The fourth cell ($13 < x < 15$ m; $10 < y < 12.5$ m) arises onshore of the bars, where the flow coming from onshore of the rip channels converges to flow offshore. The third

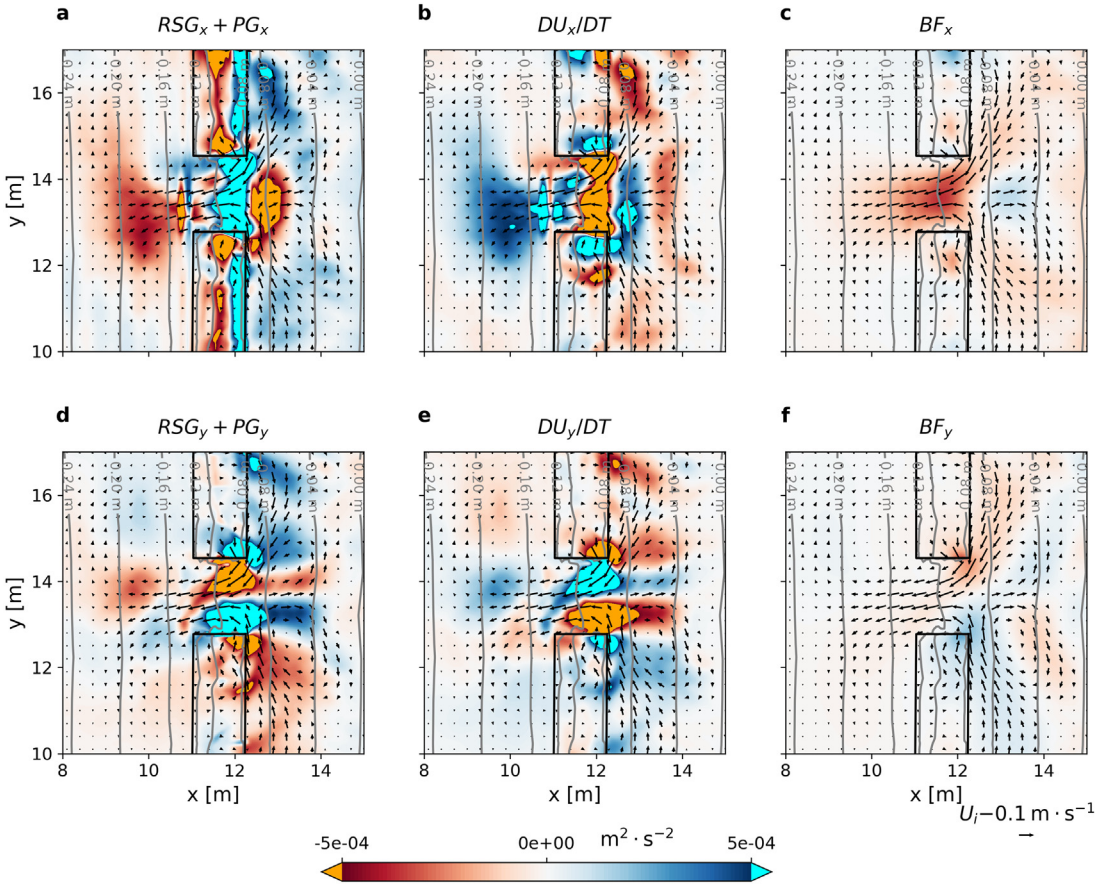

Fig. 4. Map view of depth-integrated, mean momentum terms of barred beach with rip channels (Haller et al., 2002) in the x (a–c) and y (d–f) directions: (a, d) Net of the radiation stress gradient (RSG) and pressure gradient (PG). (b, e) Total acceleration (DU_i/DT). (c, f) Bottom friction. Arrows represent the mass-flux velocity and solid grey lines give the depth contours. The solid black lines give the position of the bars. Note that colorbars exceeding the range of ± 5e–04 m^2 s^{-2} are capped at these limiting values.

and fourth cells can be thought of as similar to the first and second cells; however, they are much weaker in strength and in reverse direction (e.g., divergence behind the rips and convergence onshore of the bars).

To understand the mechanisms for this 4-cell circulation, we conducted the momentum balance analysis in both the cross-shore (x, Fig. 4a–c) and alongshore (y, Fig. 4d–e) directions. Similar to the Buckley et al. (2015) case, the magnitude of the pressure gradient (PG) and radiation stress gradient (RSG) in both the cross- and alongshore directions is large. The two terms are in near balance, but their net value provides the main driver of the mean flow (Fig. 4a, d).

The force balances in both the cross- and alongshore directions are consistent with the net of the pressure gradient and radiation stress gradient (RSG+PG, Fig. 4a,d) being balanced by the sum of the local and advective acceleration (DU/DT, Fig. 4b,e) and bottom friction (BF, Fig. 4c,f). This overall pattern is in qualitative agreement with the findings from Haller et al. (2002). The largest magnitude of momentum terms is found in the rip channel, where the strongest velocities are also observed.

The cross-shore bottom friction over the bar is a response to the onshore flow over the bar (Fig. 4c), associated with the wave breaking (first cell). The divergence of the flow over the bar towards the rip channels can be understood with the rising acceleration terms both in the x- and *y*-directions (Fig. 4b,e) associated with the alongshore pressure gradient. The confinement of the currents in the rip channels requires the rotation of the otherwise alongshore currents (second cell), coherent with very strong acceleration terms (Fig. 4b,e). Inside the rip channel, the rip currents result in a large cross-shore bottom friction (Fig. 4c) that dissipates the flow as it moves offshore. As the mechanisms of the third and fourth cell are conceptually the same as the first and second cells, they are not described here.

3.3. Comparison between internal and post-processing methods

3.3.1. Analysis of momentum balance residuals

To illustrate the differences that result from the internal and post-processing methods we calculated the momentum terms from the Buckley et al. (2015) and Haller et al. (2002) experiments with the two techniques and compared their result to the internal method.

The calculation of the momentum terms with the post-processing method consists of outputting the instantaneous water levels, pressures and depth-averaged velocities and subsequently using these to calculate each term in Eq. (9)—see Appendix B.4 for the details of the discretization method. The model setup is the same as described in Section 3.1.1, except for the output. To investigate the influence of the output time and spatial resolution, we saved the results for a range of model settings. For the Buckley et al. (2015) experiment, we adopted the finest time and spatial output resolutions corresponding to 1/40 of the peak wave period T_P and 1/40 of the peak wavelength at the outer edge of the surf zone $L_{B,P}$ (e.g., 17 Hz and 0.05 m, respectively; note that the computational grid size is 0.05 m, thus this is the finest achievable spatial resolution). As for Haller et al. (2002) experiment, we adopted the finest time and spatial output resolutions corresponding to 1/10 of the peak wave period T_P and 1/10 of the peak wavelength at the outer edge of the surf zone $L_{B,P}$ (e.g., 10 Hz and 0.10 m, respectively; note that we could not output finer resolutions due to operational storage restrictions). We also analysed the post-processing terms at half, one-quarter, one-eight and one-sixteenth of the maximum temporal and spatial resolutions (note that for the Haller et al., 2002 experiment we only analysed the half and one-quarter of the maximum resolutions due to storage constraints).

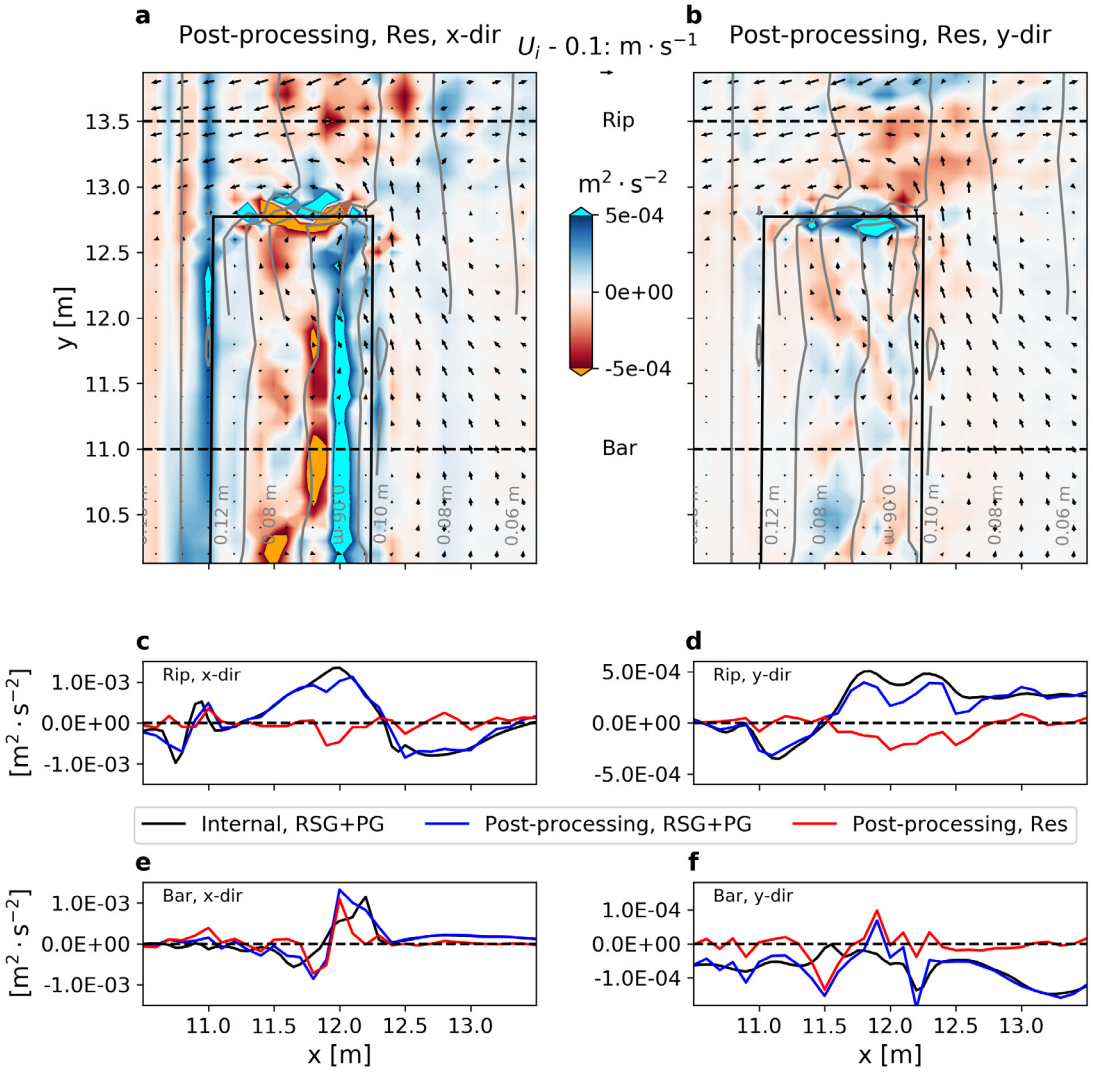

Fig. 5. Map (a, b) and cross-shore views (c–f) of depth-integrated, mean momentum terms of barred beach with rip channels using the internal and post-processing methods: (a) Residual (Res) in *x*-direction using the post-processing method. (b) Residual (Res) in *y*-direction using the post-processing method. (c–f) Net of radiation stress and pressure gradients (RSG + PG, black for internal method and blue for post-processing method) and residual (Res, red for post-processing method) in x- (c, e) and *y*-directions (d, f). Arrows represent the mass-flux velocity and solid grey lines give the depth contours. The solid black lines give the position of the bars whereas the dashed black lines provide the cross-sections used in subplots (c–f) (rip channel – (c, d) –, and bar—(e, f)). The internal residual is at computer precision and thus is not shown. Note that colorbars exceeding the range of ± 5e–04 m^2 s^{-2} are capped at these limiting values.

With the internal method described here, we are able to close the balance with a residual that is the same order as computer precision both for Buckley et al. (2015) (Fig. 2e). and Haller et al. (2002) (not shown). The residuals with the internal method are about four orders of magnitude less than those achieved with the post processing method with the finest resolution (Figs. 2e and 5).

As expected, finer time and spatial output resolutions with the post-processing method result in the decrease of the residuals (Fig. 6). For the one-dimensional case, the residuals show exponential decay with an asymptote at ~10^{-4} m^2 s^{-2}. For the two-dimensional case, the residuals are mostly flat for the spatial output and decrease for the temporal output (Fig. 6)—note that temporal and spatial resolutions higher than 10 parts per wavelength/period were not possible due to size of the output files.

Regardless of the time and spatial resolution, the residuals with the post-processing method always remained of the same order of magnitude (or larger) than the net of the pressure gradient and radiation stress gradient and its balancing terms (e.g., bottom stress; see Figs. 2c,e, 5 and 6), and four orders of magnitude larger than the internal method. For the Haller et al. (2002) experiment the fundamental mechanism driving the observed and modelled circulation was the net of radiation stress gradient and pressure gradient, thus having residuals as large as this net and its balancing terms compromises the analysis and limits the ability to understand the mean flow dynamics. In addition, the interpretation of the momentum balance with the post-processing may differ from what is calculated by the model (e.g., Fig. 5). Over the bar (11.5 < x < 12.5 m, Fig. 5e,f), the net of radiation stress and pressure gradients (RSG + PG) as predicted by both methods significantly differs, particularly in the *y*-direction (Fig. 5 f), accompanied by residuals as large as this forcing term, which impedes the analysis of the wave-flow drivers.

For the Buckley et al. (2015) experiment, as negligible mass-flux velocities were observed, the momentum balance is mainly useful to understand the wave-induced changes in the mean water level (e.g., set-down and set-up, Fig. 2b). As a result of the much simpler balance and no mean flows, applying the post-processing techniques does not change the interpretation of the momentum terms, although substantially lower precision in their calculation is achieved.

3.3.2. *Analysis of the post-processing errors*

To investigate the cause of the discrepancies between the internal and the post-processing methods, we calculated the contributions of

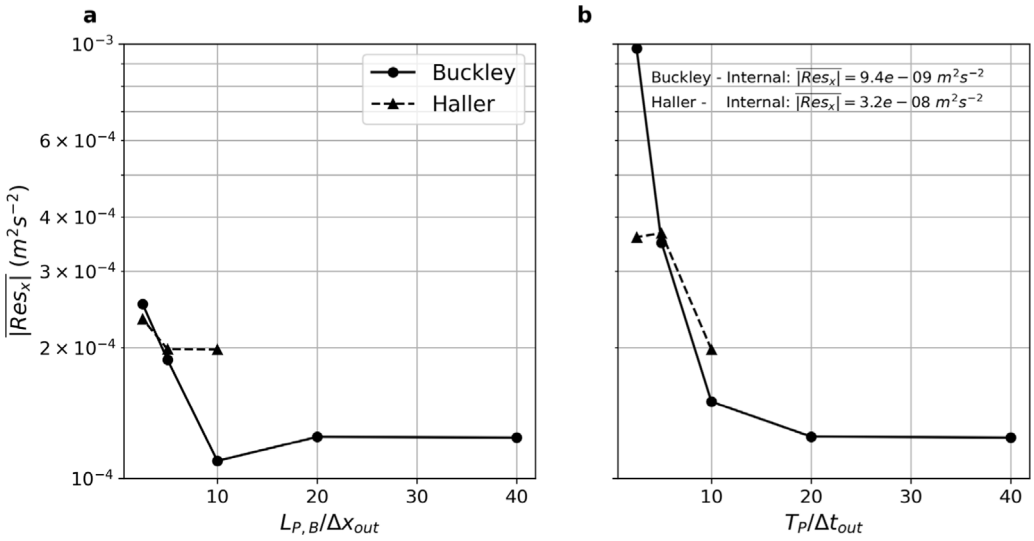

Fig. 6. Sensitivity of the mean absolute residual $|Res_x|_{mean}$ obtained with the post-processing method of Buckley et al. (2015) and Haller et al. (2002) runs to the (a) spatial and (b) temporal resolution. The spatial resolution (a) is given by the fraction of the peak wavelength at the outer edge of the surf zone $L_{P,B}$ and the output grid size Δx_{out}, whereas the temporal resolution (b) is provided by the fraction of the peak wave period T_P and the output time step Δt_{out}. Fixed temporal and spatial resolutions corresponding to the maximum values of $T_P/\Delta t_{out}$ and $L_{P,B}/\Delta x_{out}$ (e.g., equal to 40 for Buckley runs and 10 for Haller runs) are used in (a) and (b), respectively. Note that for Haller runs a fixed $L_{P,B}/\Delta y_{out}$ of 10 is used for all calculations.

each momentum term in the cross-shore direction to the total error of the post-processing method (with the finest time and spatial resolution as described above) for Buckley et al. (2015) and Haller et al. (2002) runs. To achieve this, we calculated the spatial grid average absolute error of each moment term, representing the absolute value of the difference between each momentum term calculated with the post-processing and internal (i.e., the correct value) methods, and, after adding them up, we obtained the ratio of each moment term (Fig. 7).

The largest contributions to the post-processing errors stem from the radiation stress (both orbital and pressure parts, see Eq. (10)) and pressure gradients, which are the largest momentum terms and whose mean errors are on the same order of magnitude as the residual (i.e., $\sim 10^{-4}$ m^2 s^{-2}). As the errors introduced by the remaining momentum terms (i.e., total acceleration, hydrodynamic reaction at the bottom and Reynolds stress gradients) are less than 10% (i.e., one order of magnitude or lower than the residuals—10^{-5} m^2 s^{-2}), they do not significantly contribute to the overall error of the post-processing method.

3.3.3. Evaluation of the post-processing errors

The depth-integrated mean momentum terms associated wave-induced flows are generally very small ($\sim 10^{-4}$–10^{-3} m^2 s^{-2}), therefore much smaller than their instantaneous values ($\sim 10^{-1}$–10^{0} m^2 s^{-2}). The analysis of momentum balance shows that radiation stress and pressure gradients are the largest momentum terms (10^{-3} m^2 s^{-2}), with their net (i.e., the driver of depth-integrated currents) and the secondary terms having smaller contributions (10^{-4} m^2 s^{-2}). The interpolation errors of the post-processing method, which are mainly caused by the poor representation of the radiation stress and pressure gradients, are on the same order of magnitude as the secondary momentum terms ($\sim 10^{-4}$ m^2 s^{-2}), which significantly limits the accuracy of the post processing method.

For alongshore uniform bathymetries (i.e., one-dimensional, flume cases), the set-down and set-up balance occur (i.e., pressure gradient equals radiation stress gradients, with a null net). With negligible depth-integrated velocities, the errors of the post-processing method affect the precision but not the overall interpretation of the drivers of wave-induced flow. For alongshore non-uniform bathymetries (i.e., two-dimensional, basin cases), the net of pressure and radiation stress gradients drives depth-integrated circulation, therefore the errors of the post-processing method may impact both the precision and the overall interpretation of the drivers of wave-induced flow.

4. Discussion

4.1. Depth-integrated, phase-averaged momentum balance

The internal method for calculating the depth and wave averaged momentum terms in SWASH allows for the analysis of mean flow dynamics while taking advantage of the more complete representation of the wave dynamics offered by phase-resolving models. Our motivation for developing this new approach resulted from the inaccuracy and inefficiency of post-processed methods. In Section 3.3.1, we demonstrated that the accuracy of the new method is equivalent to the precision of the numerical model, whereas with the post-processing method we are not able to close a momentum balance with sufficient precision to explain wave-induced depth-averaged currents at sites with variable bathymetry. To overcome this limitation (and the resulting impact on the interpretation of the mean flow dynamics), and to ensure that no residual remains, the calculation of the momentum terms needs to be done within the numerical model consistent with the numerical implementation of the model.

To our knowledge, this is the first effort to calculate all momentum terms at every grid and computational time step without simplification within a phase-resolving model. Previous analyses of momentum balance relied on simplifying assumptions (e.g., linear theory to calculate radiation stresses), which intrinsically limited their accuracy and application. Future investigation with our method will allow detailed analysis of the mechanisms of nearshore currents at a range of sites while taking advantage of the more realistic treatment of nonlinear processes by non-hydrostatic models.

This new methodology also results in shorter computational time and lower output storage requirements and removes the need for extensive post-processing calculations with large output files that can be prohibitive. To illustrate these added benefits of the internal over the post-processing method, we evaluated the computational time and the storage requirements of the Haller et al. (2002) simulations presented in Section 3.2. We adopted the time and spatial resolutions corresponding to 1/10 of the peak wave period T_P and 1/10 of the peak wavelength at the outer edge of the surf zone $L_{B,P}$.

The comparison (Table 4) demonstrates that the internal method has several advantages over the post-process calculations including allowing an unrestrictive spatial output resolution (i.e., similar to the numerical model), without the need for an excessive output storage, and a significantly faster total computational time.

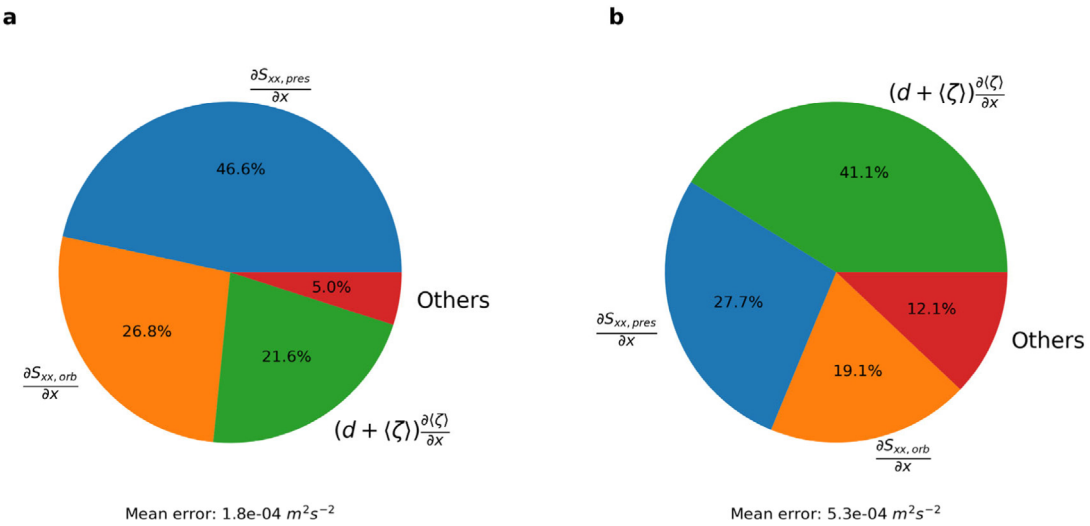

Fig. 7. Relative contribution of each momentum term in the cross-shore direction (see Eq. (9)) to the total error of the post-processing method of Buckley et al. (2015) (a) and Haller et al. (2002) (b) runs. The contributions of the total acceleration, hydrodynamic reaction at the bottom and Reynolds stress gradients were grouped as "others", as their individual contribution was each less than 10%.

Table 4
Comparison between momentum balance of barred beach with rip channels (Haller et al., 2002) calculated using post-processing and the novel method within SWASH.

Type	Variable	Symbol	Internal method	Post-processing method
Computational aspects	Number of meshes in computational grid	$mxc \mid myc$	260 | 364	
	Mesh size	Δx, Δy (m)	0.05	
	Number of vertical layers	nV	2	
	Computational time step	Δt (s)	0.01	
Output aspects	Number of meshes in output grid	$mxc_{out} \mid myc_{out}$	260 | 364	130 | 82
	Output mesh size	Δx_{out}, Δy_{out} (m)	0.05	0.10
	Output time step	Δt_{out} (s)	0.01	0.10
Calculation time	CPU time (with 36 cores)	t_{CPU} (min)	417.4	1826.4[a]
	Output processing time	t_{output} (min)	0	3.8
Storage requirement	Output size	*size* (GB)	0.01	10.32

[a]CPU time includes the time to combine the binary output files once the flow computation finishes.

4.2. Depth-integrated low-frequency momentum balance

Previously we discussed the analysis of the depth-integrated wave-averaged momentum balance, which is a powerful tool for interrogating the drivers of mean flows. By averaging over many wave periods, the wave-averaged variables (e.g., mass-flux velocity and set-up) contain information about both the high- and low-frequency components of the water level and velocities. This implies that the radiation stress term as defined in Eq. (10) is constant on the time-scale of wave groups, and thus includes both sea-swell and infragravity wave components. While useful for understanding the mean flow dynamics, this approach prevents the analysis of a range of processes, for example low frequency modulation of surf zone current. Thus, another approach is to consider the wave forcing at the wave group ('surf beat') timescale (e.g., Bertin et al., 2018; Longuet-Higgins and Stewart, 1962), which requires separating the variables into low- and high-frequency components.

To allow such an analysis we have also extended our implementation in SWASH to output the instantaneous depth-integrated momentum terms and the other instantaneous variables required for calculating mean momentum balances (as described in Section 2.3.3). Through post-processing of the instantaneous variables, it is possible to calculate the momentum balance at any time scale of interest. For the calculation of low-frequency momentum balance, we first decompose the water level and velocity signals into low-frequency ($\|\zeta\|_{lf}$, and $U_{lf,i}(x_i)$, associated with the slowly-varying flow) and high-frequency ($\zeta_{hf,i}$, and $u_{hf,i}(x_i,z,t)$, primarily associated with the short waves) components (with the cut-off frequency being based on the particular conditions or processes of interest) as follows,

$$\zeta = \|\zeta\|_{lf} + \zeta_{hf} = \zeta_{lf} + \zeta_{hf}, \tag{18}$$

$$u_i = \frac{\left\|\int_{-d}^{\zeta} u_i dz\right\|_{lf}}{d+\zeta_{lf}} + u_{hf,i} = U_{lf,i} + u_{hf,i}, \tag{19}$$

where $\|\|_{lf}$ indicates filtering with a suitable low-pass filter (e.g., a Butterworth filter). We can then compute the mean-momentum balance at the wave-group timescale,

$$\left(d+\zeta_{lf}\right)\frac{\partial U_{lf,i}}{\partial t} + \left\|U_{lf,j}\left(d+\zeta_{lf}\right)\frac{\partial U_{lf,i}}{\partial x_j}\right\|_{lf} + g\left(d+\zeta_{lf}\right)\frac{\partial \zeta_{lf}}{\partial x_i} + \frac{\partial S_{ij,lf}}{\partial x_j} + \|q_{-d}\|_{lf}\frac{\partial(-d)}{\partial x_i} = \left\|\frac{\partial\int_{-d}^{\zeta}\tau_{ij}dz}{\partial x_j}\right\|_{lf} - \|\tau_{-d,iz}\|_{lf}, \tag{20}$$

where the radiation stress $S_{ij,lf}$, is given as (e.g., Ruju et al. (2012)),

$$S_{ij,lf} = \left\|\int_{-d}^{\zeta} u_{hf,i}u_{hf,j}dz\right\|_{lf} + \left\|\int_{-d}^{\zeta} p dz\right\|_{lf} - 0.5\,g\left(d+\zeta_{lf}\right)^2. \tag{21}$$

Similar to the mean flow case (see Section 3.3.1), the key advantage of this method over a post-processing approach with the instantaneous

velocity and pressure output is that in our implementation the instantaneous momentum terms are calculated consistent with SWASH numerics, which ensures closure of the momentum balance (at computer precision). In SWASH 6.01, the user can output all depth-integrated, instantaneous momentum terms from Eq. (A.1) (see Table 2 for their correspondence with SWASH depth-integrated momentum equation, Eq. (16)), in order to compute the depth-integrated low-frequency momentum according to Eq (20).

The analysis of the low-frequency momentum balance allows for detailed investigations of the drivers of surf zone flow variations at the wave group time-scale. We expect the extension of our method for low-frequency motions to be useful not only for analysis of the momentum balance, but also for analysis of the energy balance of low-frequency waves in the nearshore (e.g., Rijnsdorp et al., 2015; Ruju et al., 2012).

5. Conclusions

In the present paper, we have presented a new method to internally calculate and extract the depth-integrated, mean momentum terms in the non-hydrostatic, phase-resolving model SWASH. The main motivation for this work was that previous attempts to close the momentum balance of phase-resolving models with post-processing techniques failed, compromising the understanding of the physical mechanisms of wave-induced currents. The core feature of the new method is its consistency with the numerical framework, which allows us to close the momentum balance with a residual that is at machine precision. By accurately calculating and extracting the momentum terms, the method provides an opportunity for advances in understanding the physics of the wave-driven, depth-averaged flows while taking advantage of the enhanced physics within phase-resolving models. We expect it to be particularly useful for sites with 2D bathymetry and flow features.

To demonstrate the utility of the new method, we applied it to two laboratory datasets, a flume case without cross-shore mass flux and a basin case with a complex 2D flow pattern. The analysis of the momentum balance terms with the internal method provided insights into the mechanisms of wave set-up and wave-driven currents. In addition, we conducted a residual analysis for the two cases both with the new method and with a post-processing approach with a range of time and spatial output resolutions. With the internal method the residuals is at computer precision, whereas with the post-processing method the residuals are on the order of the net of radiation stress gradient and pressure gradient and its balancing terms, which undermines the accuracy of the momentum balance analysis. The added advantage of the internal method over a post-processing approach is its efficiency (e.g., faster simulations and smaller output files). We have also extended the methodology to output the momentum terms at each time step, that with additional processing allows for analysis of a range of low-frequency surf zone dynamics.

The conceptualization of the method provides the general foundation for the calculation of the depth-integrated, mean momentum balances in non-hydrostatic, phase-resolving models. Although different non-hydrostatic numerical models (e.g., SWASH Zijlema et al., 2011, and NHWAVE, Ma et al., 2012) may have different numerical frameworks, the approach developed in this research could be closely replicated to accurately calculate momentum terms of wave-induced depth-averaged currents.

CRediT authorship contribution statement

Renan F. da Silva: Conceptualization, Methodology, Software, Formal analysis, Visualization, Writing – original draft, Writing – review & editing. **Dirk P. Rijnsdorp:** Conceptualization, Writing – original draft, Writing – review & editing, Supervision. **Jeff E. Hansen:** Conceptualization, Writing – original draft, Writing – review & editing, Supervision, Funding acquisition. **Ryan Lowe:** Conceptualization, Writing - original draft, Writing - review & editing, Supervision, Funding acquisition. **Mark Buckley:** Conceptualization, Writing - original draft, Writing - review & editing. **Marcel Zijlema:** Software, Writing - review & editing.

Declaration of competing interest

The authors declare that they have no known competing financial interests or personal relationships that could have appeared to influence the work reported in this paper.

Acknowledgements

This project forms part of a Ph.D. study by R.F.S. at the University of Western Australia which is supported by the Commonwealth Government through an Australian Government Research Training Program Scholarship. Parts of this research were also supported by the Wave Energy Research Centre through funding provided by the Western Australian Government, via the Department of Primary Industries and Regional Development (DPIRD), and University of Western Australia. Additional support was also provided from the Australian Renewable Energy Agency, Research and Development Programme (grant number 2015RND086). This work was also supported by resources provided by the Pawsey Supercomputing Centre with funding from the Australian Government, Government of Western Australia and the University of Western Australia. We would like to thank Adria Elskus (USGS), the editor and the five anonymous reviewers for their constructive reviews that improved this manuscript.

Appendix A. Derivation of the depth-integrated, phase-averaged momentum equation

The derivation of the depth-integrated, mean momentum equation consists of: the depth- and time-integrations of the RANS equations, Eqs. (1) and (2); next, we decompose the velocity signal into the mean flow and wave velocities, Eqs. (7) and (8); subsequently, we rewrite the depth and time-integrated momentum equation using the depth and time-integrated continuity equation and decomposed velocities.

The depth-integration of the continuity equation results in the global continuity equation, Eq. (6). The depth-integration of the horizontal momentum balance equation in divergence form, Eq. (2), results in the following,

$$\frac{\partial \int_{-d}^{\zeta} u_i dz}{\partial t} + \frac{\partial \int_{-d}^{\zeta} u_i u_j dz}{\partial x_j} + \frac{\partial \int_{-d}^{\zeta} p\, dz}{\partial x_i} + p_{-d}\frac{\partial(-d)}{\partial x_i} = \frac{\partial \int_{-d}^{\zeta} \tau_{ij} dz}{\partial x_j} - \tau_{-d,iz}. \tag{A.1}$$

The time-integration over many wave periods of the global continuity and horizontal momentum balance equations, Eqs. (6) and (A.1), results in the following,

$$\left\langle \frac{\partial \zeta}{\partial t} \right\rangle + \left\langle \frac{\partial \int_{-d}^{\zeta} u_j dz}{\partial x_j} \right\rangle = 0, \tag{A.2}$$

$$\left\langle \frac{\partial \int_{-d}^{\zeta} u_i dz}{\partial t} \right\rangle + \left\langle \frac{\partial \int_{-d}^{\zeta} u_i u_j dz}{\partial x_j} \right\rangle + \left\langle \frac{\partial \int_{-d}^{\zeta} p\, dz}{\partial x_i} \right\rangle + \langle p_{-d} \rangle \frac{\partial(-d)}{\partial x_i} = \left\langle \frac{\partial \int_{-d}^{\zeta} \tau_{ij} dz}{\partial x_j} \right\rangle - \langle \tau_{-d,iz} \rangle. \tag{A.3}$$

Next, the previously defined mass flux velocity U_i, Eq. (7), and the oscillatory velocity $\widetilde{u_i}$, Eq. (8) are used to rewrite Eqs. (A.2) and (A.3). Eq. (A.2) thus becomes,

$$\left\langle \frac{\partial \zeta}{\partial t} \right\rangle + \frac{\partial \left[U_j (d + \langle \zeta \rangle)\right]}{\partial x_j} = 0. \tag{A.4}$$

As for Eq. (A.3), we first present the time-integration for each term separately, and then combine them in a single equation. By assuming a stationary flow ($\partial U_i/\partial t = 0$) the local acceleration is written as,

$$\left\langle \frac{\partial \int_{-d}^{\zeta} u_i dz}{\partial t} \right\rangle = U_i \left\langle \frac{\partial (d+\zeta)}{\partial t} \right\rangle + \left\langle \frac{\partial \int_{-d}^{\zeta} \widetilde{u_i} dz}{\partial t} \right\rangle. \tag{A.5}$$

By combining Eqs. (A.4) and (A.5), the local acceleration is rewritten as,

$$\left\langle \frac{\partial \int_{-d}^{\zeta} u_i dz}{\partial t} \right\rangle = -U_i \left[\frac{\partial \left[U_j \left(d + \langle \zeta \rangle \right) \right]}{\partial x_j} \right] + \left\langle \frac{\partial \int_{-d}^{\zeta} \widetilde{u}_i dz}{\partial t} \right\rangle. \tag{A.6}$$

Next, the advective acceleration is rewritten as follows,

$$\begin{aligned} \left\langle \frac{\partial \int_{-d}^{\zeta} u_i u_j dz}{\partial x_j} \right\rangle & \\ = U_i \left[\frac{\partial \left[U_j \left(d + \langle \zeta \rangle \right) \right]}{\partial x_j} \right] + \left(d + \langle \zeta \rangle \right) U_j \frac{\partial U_i}{\partial x_j} & \\ + \frac{\partial \left\langle \int_{-d}^{\zeta} \widetilde{u}_i \widetilde{u}_j dz \right\rangle}{\partial x_i}. & \end{aligned} \tag{A.7}$$

As for the pressure term, firstly we separate the mean pressure at the bottom into a hydrostatic and non-hydrostatic part (q), which equals the dynamic pressure at the bottom used by Mei et al. (2005), as follows,

$$\langle p_{-d} \rangle = g \left(d + \langle \zeta \rangle \right) + \langle q_{-d} \rangle. \tag{A.8}$$

Accordingly, the slope term can be rewritten as,

$$\begin{aligned} \langle p_{-d} \rangle \frac{\partial (-d)}{\partial x_i} & = g \left(d + \langle \zeta \rangle \right) \frac{\partial (-d)}{\partial x_i} + \langle q_{-d} \rangle \frac{\partial (-d)}{\partial x_i} + g \left(d + \langle \zeta \rangle \right) \frac{\partial \langle \zeta \rangle}{\partial x_i} \\ & - g \left(d + \langle \zeta \rangle \right) \frac{\partial \langle \zeta \rangle}{\partial x_i}. \end{aligned} \tag{A.9}$$

Consequently, it follows that,

$$\langle p_{-d} \rangle \frac{\partial (-d)}{\partial x_i} = g \left(d + \langle \zeta \rangle \right) \frac{\partial \langle \zeta \rangle}{\partial x_i} - \frac{g}{2} \frac{\partial \left(d + \langle \zeta \rangle \right)^2}{\partial x_i} + \langle q_{-d} \rangle \frac{\partial (-d)}{\partial x_i}. \tag{A.10}$$

The total pressure term is finally calculated as,

$$\begin{aligned} & \frac{\partial \left\langle \int_{-d}^{\zeta} p \, dz \right\rangle}{\partial x_i} + \langle p_{-d} \rangle \frac{\partial (-d)}{\partial x_i} \\ & = g \left(d + \langle \zeta \rangle \right) \frac{\partial \langle \zeta \rangle}{\partial x_i} + \frac{\partial \left[\left\langle \int_{-d}^{\zeta} p \, dz \right\rangle - 0.5 \, g \left(d + \langle \zeta \rangle \right)^2 \right]}{\partial x_i} + \langle q_{-d} \rangle \frac{\partial (-d)}{\partial x_i}. \end{aligned} \tag{A.11}$$

By adding the above derived terms in Eqs. (A.6), (A.7) and (A.11), Eq. (A.3) becomes,

$$\begin{aligned} \left\langle \frac{\partial \int_{-d}^{\zeta} \widetilde{u}_i dz}{\partial t} \right\rangle & + \left(d + \langle \zeta \rangle \right) U_j \frac{\partial U_i}{\partial x_j} + g \left(d + \langle \zeta \rangle \right) \frac{\partial \langle \zeta \rangle}{\partial x_i} + \frac{\partial \left\langle \int_{-d}^{\zeta} \widetilde{u}_i \widetilde{u}_j dz \right\rangle}{\partial x_i} \\ & + \frac{\partial \left[\left\langle \int_{-d}^{\zeta} p \, dz \right\rangle - 0.5 \, g \left(\langle \zeta \rangle + d \right)^2 \right]}{\partial x_i} + \langle q_{-d} \rangle \frac{\partial (-d)}{\partial x_i} \\ & = \frac{\partial \left\langle \int_{-d}^{\zeta} \tau_{ij} dz \right\rangle}{\partial x_j} - \left\langle \tau_{-d,iz} \right\rangle. \end{aligned} \tag{A.12}$$

The final step of the derivation consists of rewriting Eq. (A.12) with Eq. (10) and results in Eq. (9).

Appendix B. SWASH framework

B.1. Derivation of SWASH layer-averaged momentum equation

The steps to derive SWASH layer-averaged momentum equation, Eq. (11), from the primitive RANS equations, Eqs. (1) and (2), consist of: layer integration of the horizontal momentum equation, Eq. (2), which is in divergence form; next, to convert it to an advective form, we rewrite the layer-integrated horizontal momentum equation in flux form using the layer-integrated continuity equation.

The integration by vertical layers of Eq. (2) - neglecting for simplicity the Reynolds stress gradients – starts as follows,

$$\begin{aligned} \int_{z_{k-1/2}}^{z_{k+1/2}} \frac{\partial u}{\partial t} dz + \int_{z_{k-1/2}}^{z_{k+1/2}} \frac{\partial uu}{\partial x} dz + \int_{z_{k-1/2}}^{z_{k+1/2}} \frac{\partial wu}{\partial z} dz & \\ + \int_{z_{k-1/2}}^{z_{k+1/2}} \frac{\partial p}{\partial x} dz = 0. & \end{aligned} \tag{B.1}$$

We first derive each term of Eq. (B.1) separately, and further combine them in a single equation. The local acceleration term is given by,

$$\int_{z_{k-1/2}}^{z_{k+1/2}} \frac{\partial u}{\partial t} dz = u_k \frac{\partial h_k}{\partial t} + h_k \frac{\partial u_k}{\partial t} - \overline{u}^z_{k+1/2} \frac{\partial z_{k+1/2}}{\partial t} + \overline{u}^z_{k-1/2} \frac{\partial z_{k-1/2}}{\partial t}. \tag{B.2}$$

The horizontal advective acceleration term is expanded as follows,

$$\begin{aligned} \int_{z_{k-1/2}}^{z_{k+1/2}} \frac{\partial uu}{\partial x} dz = \frac{\partial h_k u_k^2}{\partial x} - \overline{u}^z_{k+1/2} \overline{u}^z_{k+1/2} \frac{\partial z_{k+1/2}}{\partial x} & \\ + \overline{u}^z_{k-1/2} \overline{u}^z_{k-1/2} \frac{\partial z_{k-1/2}}{\partial x}. & \end{aligned} \tag{B.3}$$

The vertical advective acceleration is given by,

$$\int_{z_{k-1/2}}^{z_{k+1/2}} \frac{\partial wu}{\partial z} dz = w_{k+1/2} \overline{u}^z_{k+1/2} - w_{k-1/2} \overline{u}^z_{k-1/2}. \tag{B.4}$$

As for the pressure term (p), firstly we separate it into the hydrostatic $[g(\zeta - z)]$ and non-hydrostatic part (q) as follows,

$$\int_{z_{k-1/2}}^{z_{k+1/2}} \frac{\partial p}{\partial x} dz = g \int_{z_{k-1/2}}^{z_{k+1/2}} \frac{\partial (\zeta - z)}{\partial x} dz + \int_{z_{k-1/2}}^{z_{k+1/2}} \frac{\partial q}{\partial x} dz. \tag{B.5}$$

Thus, the pressure terms can be written as,

$$\int_{z_{k-1/2}}^{z_{k+1/2}} \frac{\partial p}{\partial x} dz = g h_k \frac{\partial \zeta}{\partial x} + \frac{\partial h_k \overline{q}^z_k}{\partial x} - q_{k+1/2} \frac{\partial z_{k+1/2}}{\partial x} + q_{k-1/2} \frac{\partial z_{k-1/2}}{\partial x}. \tag{B.6}$$

By adding all previous terms in Eqs. (B.2), (B.3), (B.4) and (B.6), (B.1) becomes,

$$\begin{aligned} u_k \frac{\partial h_k}{\partial t} + h_k \frac{\partial u_k}{\partial t} + \frac{\partial \phi_k u_k}{\partial x} + \overline{u}^z_{k+1/2} \omega_{k+1/2} - \overline{u}^z_{k-1/2} \omega_{k-1/2} + g h_k \frac{\partial \zeta}{\partial x} & \\ + \frac{\partial h_k \overline{q}^z_k}{\partial x} - q_{k+1/2} \frac{\partial z_{k+1/2}}{\partial x} + q_{k-1/2} \frac{\partial z_{k-1/2}}{\partial x} = 0. & \end{aligned} \tag{B.7}$$

To convert the layer-integrated momentum equation in divergence form, Eq. (B.7), to the advective form, we first need to define the layer-integrated continuity equation that is obtained through the integration of the local continuity equation over a vertical layer,

$$\begin{aligned} \int_{z_{k-1/2}}^{z_{k+1/2}} \frac{\partial u}{\partial x} dz + \int_{z_{k-1/2}}^{z_{k+1/2}} \frac{\partial w}{\partial z} dz & \\ = \frac{\partial \int_{z_{k-1/2}}^{z_{k+1/2}} u \, dz}{\partial x} - \overline{u}^z_{k+1/2} \frac{\partial z_{k+1/2}}{\partial x} + \overline{u}^z_{k-1/2} \frac{\partial z_{k-1/2}}{\partial x} & \\ + w_{k+1/2} - w_{k-1/2} = 0. & \end{aligned} \tag{B.8}$$

Eq. (B.8) can be rewritten using the mass flux ϕ and the relative vertical velocity ω as follows,

$$\frac{\partial h_k}{\partial t} + \frac{\partial \phi_k}{\partial x} + \omega_{k+1/2} - \omega_{k-1/2} = 0. \tag{B.9}$$

Next, we subtract the product of the local continuity equation, Eq. (B.9), and the horizontal velocity u_k from the layer-integrated momentum equation, Eq. (B.7), and divide it by the layer thickness h_k,

which results in,

$$\overbrace{\frac{u_k}{h_k}\frac{\partial h_k}{\partial t}-\frac{u_k}{h_k}\frac{\partial h_k}{\partial t}}^{=0}+\frac{\partial u_k}{\partial t}+\frac{1}{h_k}\left(\frac{\partial \phi_k u_k}{\partial x}-u_k\frac{\partial \phi_k}{\partial x}\right)$$
$$+\frac{1}{h_k}\left(\overline{u}^z_{k+1/2}\omega_{k+1/2}-\overline{u}^z_{k-1/2}\omega_{k-1/2}-u_k\omega_{k+1/2}\right.$$
$$\left.+u_k\omega_{k-1/2}\right)+g\frac{\partial \zeta}{\partial x}+\frac{1}{h_k}\frac{\partial h_k\overline{q}^z_{k+1/2}}{\partial x}-\frac{q_{k+1/2}}{h_k}\frac{\partial z_{k+1/2}}{\partial x}$$
$$+\frac{q_{k-1/2}}{h_k}\frac{\partial z_{k-1/2}}{\partial x}=0. \tag{B.10}$$

B.2. Derivation of SWASH depth-integrated momentum equation

Eq. (B.10) provides the layer-averaged momentum equation in the advective form as efficiently solved by SWASH. However, to be able to extract the momentum terms from SWASH in a manner consistent with depth-integrated, mean momentum equation in advective form, Eq. (9), we need to use the layer-integrated equation in the flux form, Eq. (B.7). This occurs due to the need of holding the term $u_k\frac{\partial h_k}{\partial t}$ that partially contributes to the depth-integrated local acceleration and to the advective acceleration momentum terms and thus cannot be cancelled.

To reach Eq. (B.7) from Eq. (B.10), we need to follow the opposite way, namely, we first multiply Eq. (B.10) by the layer thickness h_k, and then add the product of the local continuity equation, Eq. (B.9), and the layer-averaged velocity u_k. To obtain the SWASH instantaneous depth-integrated momentum equation in a manner consistent with Eq. (A.1), we integrate Eq. (B.7) in the vertical through the sum of the layer-integrated momentum terms as follows,

$$\sum_{k=1}^{k=K}\left[u_k\frac{\partial h_k}{\partial t}+h_k\frac{\partial u_k}{\partial t}\right]+\sum_{k=1}^{k=K}\frac{\partial \phi_k u_k}{\partial x}+\sum_{k=1}^{k=K}\left[gh_k\frac{\partial \zeta}{\partial x}+\frac{\partial h_k\overline{q}^z_{k+1/2}}{\partial x}\right]$$
$$-q_{-d}\frac{\partial d}{\partial x}=0, \tag{B.11}$$

where we notice that the depth-integration of Eq. (B.7) results in the cancelling of some terms (e.g., $(\sum_{k=1}^{k=K}\left[\overline{u}^z_{k+1/2}\omega_{k+1/2}-\overline{u}^z_{k-1/2}\omega_{k-1/2}\right]=0$).

The comparison term-by-term of the SWASH depth-integrated momentum equation, Eq. (B.11), with the depth-integrated momentum equation, Eq. (A.1), is presented in Table 2.

B.3. Numerical framework of SWASH

In this section, we only present the discretization of the equations relevant for the extraction of the depth-integrated momentum terms, namely, the layer-averaged momentum equation, Eq. (11) and the local continuity equation, Eq. (B.9). Further details of the SWASH implementation can be found in e.g., Zijlema and Stelling (2008).

An explicit, second order finite difference method for staggered grids is used in SWASH. The horizontal velocities are positioned at the horizontal grid corners and vertical centres ($u_{i+1/2,k}$), whereas the vertical velocities are positioned at the vertical grid corners and horizontal centres ($w_{i,k+1/2}$, see Fig. 1). The water levels are prescribed at the horizontal grid centre (ζ_i). For the non-hydrostatic pressure, the user can choose between two discretization methods, that is, the standard method, for which the non-hydrostatic pressures are at the horizontal and vertical centres ($q_{i,k}$), and Keller-box method (Lam and Simpson, 1976), for which they are at the horizontal grid centre but at the vertical corners ($q_{i,k+1/2}$). Here for the purpose of wave computations we present the discretization with the Keller-box method. The continuity and horizontal momentum equations are solved at the horizontal grid centres ($x_{i+1/2,k}$) and corners ($x_{i,k}$), respectively, with a $\Delta x/2$ difference in the horizontal.

As for the time integration, the user needs to choose between the second-order leapfrog scheme and the θ-method. For the leapfrog scheme, the time stamp of the velocities and water level and pressures differ by $\Delta t/2$, with Δt being the time step (e.g., $u,w^{n+1/2}$ and ζ^n), whereas they are at the same for the θ-method (e.g., u,w^n and ζ^n). The discretization of the water-level gradient term in the layer-averaged momentum equation, Eq. (11), depends on the chosen method, namely, the leapfrog scheme calculates it explicitly and the θ-method solves it implicitly. For both methods, the horizontal advective and Reynolds stress horizontal gradients terms are solved explicitly, whereas the vertical terms (e.g., vertical advective and Reynolds stress vertical gradients) and non-hydrostatic pressure terms are calculated implicitly.

We only present the implementation of the leapfrog scheme because of its relevance for the simulation of gravity waves. The discretization of the layer-averaged momentum equation, Eq. (11), for the leapfrog scheme is shown below,

$$\frac{u^{n+1/2}_{i+1/2,k}-u^{n-1/2}_{i+1/2,k}}{\Delta t}$$
$$+\frac{1}{\left(\overline{h}^x_{i+1/2,k}\right)^n}\left(\frac{\overline{\phi}^n_{i+1,k}\left(\hat{u}^{n-1/2}_{i+1,k}-u^{n-1/2}_{i+1/2,k}\right)-\overline{\phi}^n_{i,k}\left(\hat{u}^{n-1/2}_{i,k}-u^{n-1/2}_{i+1/2,k}\right)}{\Delta x}\right)$$
$$+\frac{\left(\overline{\omega}^x_{i+1/2,k+1/2}\right)^{n-1/2}}{\left(\overline{h}^x_{i+1/2,k}\right)^n}\left(\left(\overline{u}^z_{i+1/2,k+1/2}\right)^{n-1/2+\theta_u}-u^{n-1/2+\theta_u}_{i+1/2,k}\right)$$
$$-\frac{\left(\overline{\omega}^x_{i+1/2,k-1/2}\right)^{n-1/2}}{\left(\overline{h}^x_{i+1/2,k}\right)^n}\left(\left(\overline{u}^z_{i+1/2,k-1/2}\right)^{n-1/2+\theta_u}-u^{n-1/2+\theta_u}_{i+1/2,k}\right)$$
$$+g\frac{\zeta^n_{i+1}-\zeta^n_i}{\Delta x}+\frac{1}{\left(\overline{h}^x_{i+1/2,k}\right)^n}\left(\frac{h^n_{i+1,k}\left(\overline{q}^z_{i+1,k}\right)^{n+1}-h^n_{i,k}\left(\overline{q}^z_{i,k}\right)^{n+1}}{\Delta x}\right)$$
$$-\frac{\left(\overline{q}^x_{i+1/2,k+1/2}\right)^{n+1}}{\left(\overline{h}^x_{i+1/2,k}\right)^n}\frac{z^n_{i+1,k+1/2}-z^n_{i,k+1/2}}{\Delta x}$$
$$+\frac{\left(\overline{q}^x_{i+1/2,k-1/2}\right)^{n+1}}{\left(\overline{h}^x_{i+1/2,k}\right)^n}\frac{z^n_{i+1,k-1/2}-z^n_{i,k-1/2}}{\Delta x}=0, \tag{B.12}$$

where θ_u is the parameter for the θ-method (between 0 and 1, with 0.5 and 1 corresponding to the second order Crank–Nicolson and first order implicit Euler scheme, respectively; for brevity, we write $\varphi^{n+\theta}=\theta\varphi^{n+1}+(1-\theta)\varphi^n$). The upwind horizontal velocity $\hat{u}^{n-1/2}_{i+1,k}$ is approximated second order accurately as

$$\hat{u}^{n-1/2}_{i,k}=\begin{cases}\frac{3}{2}u_{i-1/2,k}-\frac{1}{2}u_{i-3/2,k}, & if\left(\overline{\phi}^x_{i,k}\right)^{n-1/2}\geq 0\\ \frac{3}{2}u_{i+1/2,k}-\frac{1}{2}u_{i+3/2,k}, & if\left(\overline{\phi}^x_{i,k}\right)^{n-1/2}<0.\end{cases} \tag{B.13}$$

It should be noted that the obtained numerical approximations, Eqs. (B.12) and (B.13), essentially inherit the physical properties of the momentum balance because of the staggered framework employing the momentum-conservative scheme of Stelling and Duinmeijer (2003). See also Zijlema and Stelling (2008) and Zijlema (2019) for details. This implies that the effect of discretization error is limited, in that the overall balance between various momentum contribution terms is merely influenced by the mesh resolution.

The relative vertical velocity $\omega^{n-1/2}_{i,k+1/2}$ is defined by,

$$\begin{aligned}&\omega^{n-1/2}_{i,k+1/2}\\&= w^{n-1/2}_{i,k+1/2} - \frac{z^{n}_{i,k+1/2} - z^{n-1}_{i,k+1/2}}{\Delta t}\\&-\left(\frac{\left(\overline{u}^{x}_{i,k}\right)^{n-1/2} h^{n-1}_{i,k+1} + \left(\overline{u}^{x}_{i,k+1}\right)^{n-1/2} h^{n-1}_{i,k}}{h^{n-1}_{i,k} + h^{n-1}_{i,k+1}}\right)\\&\times \frac{\left(\overline{z}^{x}_{i+1/2,k+1/2}\right)^{n-1} - \left(\overline{z}^{x}_{i-1/2,k+1/2}\right)^{n-1}}{\Delta x}.\end{aligned} \tag{B.14}$$

The local mass flux $\phi^{n-1/2}_{i+1/2,k}$ is the speed with which both mass and momentum are transported and is provided by,

$$\phi^{n-1/2}_{i+1/2,k} = \hat{h}^{n-1}_{i+1/2,k} u^{n-1/2}_{i+1/2,k}, \tag{B.15}$$

with the upwind layer thickness being defined by $\hat{h}^{n}_{i+1/2,k} = f_k \hat{H}^{n}_{i+1/2}$, where the upwind depth is given by,

$$\hat{H}^{n}_{i+1/2} = \begin{cases}\zeta^{n}_{i} + d_i, & if \ \sum_{k=1}^{k=K} u^{n-1/2}_{i+1/2,k} \hat{h}^{n-1}_{i+1/2,k} > 0\\ \zeta^{n}_{i+1} + \mathrm{d}_{i+1}, & if \ \sum_{k=1}^{k=K} u^{n-1/2}_{i+1/2,k} \hat{h}^{n-1}_{i+1/2,k} < 0\\ \max\left(\zeta_i, \zeta_{i+1}\right) + \min\left(d_i, d_{i+1}\right), & if \ \sum_{k=1}^{k=K} u^{n-1/2}_{i+1/2,k} \hat{h}^{n-1}_{i+1/2,k} = 0.\end{cases} \tag{B.16}$$

The solution procedure of SWASH gives rise to two new terms in the layer-averaged momentum equation, Eq. (B.12). The first term adds to the horizontal advective terms and originates from the MacCormack predictor–corrector technique (see Zijlema et al., 2011 for details). The second term adds to the non-hydrostatic pressure gradient terms, and comes from the pressure correction technique to solve the non-hydrostatic pressure. The non-hydrostatic pressure gradient term is first assumed to be at the previous time stamp, and it is corrected after solving the non-hydrostatic pressure gradient variation through the Poisson equation (see Zijlema and Stelling, 2005 for details). The two new terms are calculated in steps, where for each new step an intermediate velocity is obtained, and as such they include the contribution from the implicit (i.e., with θ_u) vertical terms (see below). The final layer-averaged momentum including these contributions reads,

$$\begin{aligned}&\frac{u^{n+1/2}_{i+1/2,k} - u^{n-1/2}_{i+1/2,k}}{\Delta t}\\&+\frac{1}{\left(\overline{h}^{x}_{i+1/2,k}\right)^{n}}\left(\frac{\overline{\phi}^{n}_{i+1,k}\left(\hat{u}^{n-1/2}_{i+1,k} - u^{n-1/2}_{i+1/2,k}\right) - \overline{\phi}^{n}_{i,k}\left(\hat{u}^{n-1/2}_{i,k} - u^{n-1/2}_{i+1/2,k}\right)}{\Delta x}\right)\\&+\frac{\Delta t}{\left(\overline{h}^{x}_{i+1/2,k}\right)^{n}}\left(\frac{\overline{\phi}^{n-1/2}_{i+1,k}\overline{\Delta u}^{x}_{i+1,k} - \overline{\phi}^{n-1/2}_{i,k}\overline{\Delta u}^{x}_{i,k}}{\Delta x}\right)\left(\frac{1}{\Delta \mathrm{t}}\right.\\&\left.-\theta_u\frac{\left(\overline{\omega}^{x}_{i+1/2,k+1/2}\right)^{n-1/2}}{\left(\overline{h}^{x}_{i+1/2,k}\right)^{n}} + \theta_u\frac{\left(\overline{\omega}^{x}_{i+1/2,k-1/2}\right)^{n-1/2}}{\left(\overline{h}^{x}_{i+1/2,k}\right)^{n}}\right)\\&+\frac{\left(\overline{\omega}^{x}_{i+1/2,k+1/2}\right)^{n-1/2}}{\left(\overline{h}^{x}_{i+1/2,k}\right)^{n}}\left(\left(\overline{u}^{z}_{i+1/2,k+1/2}\right)^{n-1/2+\theta_u} - u^{n-1/2+\theta_u}_{i+1/2,k}\right)\\&-\frac{\left(\overline{\omega}^{x}_{i+1/2,k-1/2}\right)^{n-1/2}}{\left(\overline{h}^{x}_{i+1/2,k}\right)^{n}}\left(\left(\overline{u}^{z}_{i+1/2,k-1/2}\right)^{n-1/2+\theta_u} - u^{n-1/2+\theta_u}_{i+1/2,k}\right)\end{aligned}$$

$$\begin{aligned}&+g\frac{\zeta^{n}_{i+1} - \zeta^{n}_{i}}{\Delta x} + \frac{1}{\left(\overline{h}^{x}_{i+1/2,k}\right)^{n}}\left(\frac{h^{n}_{i+1,k}\left(\overline{q}^{z}_{i+1,k}\right)^{n} - h^{n}_{i,k}\left(\overline{q}^{z}_{i,k}\right)^{n}}{\Delta x}\right)\\&-\frac{\left(\overline{q}^{x}_{i+1/2,k+1/2}\right)^{n}}{\left(\overline{h}^{x}_{i+1/2,k}\right)^{n}}\frac{z^{n}_{i+1,k+1/2} - z^{n}_{i,k+1/2}}{\Delta x}\\&+\frac{\left(\overline{q}^{x}_{i+1/2,k-1/2}\right)^{n}}{\left(\overline{h}^{x}_{i+1/2,k}\right)^{n}}\frac{z^{n}_{i+1,k-1/2} - z^{n}_{i,k-1/2}}{\Delta x}\\&+\left(\frac{1}{\left(\overline{h}^{x}_{i+1/2,k}\right)^{n}}\left(\frac{h^{n}_{i+1,k}\overline{\Delta q}^{z}_{i+1,k} - h^{n}_{i,k}\overline{\Delta q}^{z}_{i,k}}{\Delta x}\right)\right.\\&-\frac{\overline{\Delta q}^{x}_{i+1/2,k+1/2}}{\left(\overline{h}^{x}_{i+1/2,k}\right)^{n}}\frac{z^{n}_{i+1,k+1/2} - z^{n}_{i,k+1/2}}{\Delta x}\\&\left.+\frac{\overline{\Delta q}^{x}_{i+1/2,k-1/2}}{\left(\overline{h}^{x}_{i+1/2,k}\right)^{n}}\frac{z^{n}_{i+1,k-1/2} - z^{n}_{i,k-1/2}}{\Delta x}\right)\left(\frac{1}{\Delta \mathrm{t}} - \theta_u\frac{\left(\overline{\omega}^{x}_{i+1/2,k+1/2}\right)^{n-1/2}}{\left(\overline{h}^{x}_{i+1/2,k}\right)^{n}}\right.\\&\left.+\theta_u\frac{\left(\overline{\omega}^{x}_{i+1/2,k-1/2}\right)^{n-1/2}}{\left(\overline{h}^{x}_{i+1/2,k}\right)^{n}}\right) = 0,\end{aligned} \tag{B.17}$$

where the velocity correction reads as follows,

$$\Delta u_{i+1,k} = \begin{cases}\frac{1}{2}\left(u^{*}_{i-1/2,k} - u^{n-1/2}_{i-3/2,k}\right), & if \ \left(\overline{\phi}^{x}_{i+1,k}\right)^{n-1/2} \geq 0\\ \frac{1}{2}\left(u^{n-1/2}_{i+1/2,k} - u^{*}_{i+3/2,k}\right), & if \ \left(\overline{\phi}^{x}_{i+1,k}\right)^{n-1/2} < 0,\end{cases} \tag{B.18}$$

where u^* is an intermediate value calculated with,

$$\begin{aligned}&\frac{u^{*}_{i+1/2,k} - u^{n-1/2}_{i+1/2,k}}{\Delta t}\\&+\frac{1}{\left(\overline{h}^{x}_{i+1/2,k}\right)^{n}}\left(\frac{\overline{\phi}^{n}_{i+1,k}\left(\hat{u}^{n-1/2}_{i+1,k} - u^{n-1/2}_{i+1/2,k}\right) - \overline{\phi}^{n}_{i,k}\left(\hat{u}^{n-1/2}_{i,k} - u^{n-1/2}_{i+1/2,k}\right)}{\Delta x}\right)\\&+\frac{\left(\overline{\omega}^{x}_{i+1/2,k+1/2}\right)^{n-1/2}}{\left(\overline{h}^{x}_{i+1/2,k}\right)^{n}}\left(\left(\overline{u}^{z}_{i+1/2,k+1/2}\right)^{n-1/2+\theta_u} - u^{n-1/2+\theta_u}_{i+1/2,k}\right)\\&-\frac{\left(\overline{\omega}^{x}_{i+1/2,k-1/2}\right)^{n-1/2}}{\left(\overline{h}^{x}_{i+1/2,k}\right)^{n}}\left(\left(\overline{u}^{z}_{i+1/,k-1/2}\right)^{n-1/2+\theta_u} - u^{n-1/2+\theta_u}_{i+1/2,k}\right)\\&+g\frac{\zeta^{n}_{i+1} - \zeta^{n}_{i}}{\Delta x} + \frac{1}{\left(\overline{h}^{x}_{i+1/2,k}\right)^{n}}\left(\frac{h^{n}_{i+1,k}\left(\overline{q}^{z}_{i+1,k}\right)^{n} - h^{n}_{i,k}\left(\overline{q}^{z}_{i,k}\right)^{n}}{\Delta x}\right)\\&-\frac{\left(\overline{q}^{x}_{i+1/2,k+1/2}\right)^{n}}{\left(\overline{h}^{x}_{i+1/2,k}\right)^{n}}\frac{z^{n}_{i+1,k+1/2} - z^{n}_{i,k+1/2}}{\Delta x}\\&+\frac{\left(\overline{q}^{x}_{i+1/2,k-1/2}\right)^{n}}{\left(\overline{h}^{x}_{i+1/2,k}\right)^{n}}\frac{z^{n}_{i+1,k-1/2} - z^{n}_{i,k-1/2}}{\Delta x} = 0.\end{aligned} \tag{B.19}$$

The non-hydrostatic pressure at the new time level $q^{n+1}_{i,k+1/2}$ is given by $q^{n}_{i,k+1/2} + \Delta q_{i,k+1/2}$, with the last term calculated through the Poisson equation (not shown).

Although the local continuity is not directly solved in SWASH for non-hydrostatic simulations, the conversion of the layer-averaged momentum equation in the advective form, Eq. (11), to the flux form, Eq. (B.7), requires its definition (see Appendix B.1). Here we assume the following discretization for the local continuity equation (Zijlema

and Stelling, 2008),

$$\frac{\left(\overline{h}^{x}_{i+1/2,k}\right)^{n+1}-\left(\overline{h}^{x}_{i+1/2,k}\right)^{n}}{\Delta t}+\frac{\hat{h}^{n}_{i+1/2,k}u^{n+1/2}_{i+1/2,k}-\hat{h}^{n}_{i-1/2,k}u^{n+1/2}_{i-1/2,k}}{\Delta x}+\left(\overline{\omega}^{x}_{i+1/2,k+1/2}\right)^{n+1/2}-\left(\overline{\omega}^{x}_{i+1/2,k-1/2}\right)^{n+1/2}=0. \tag{B.20}$$

B.4. Post-processing method

In this section, we present the post-processing method for calculating the depth-integrated phase-averaged momentum terms. For simplicity, we only show the implementation for SWASH 2DV (i.e., similar to our modelling of Buckley et al. (2015)'s experiment).

We output all variables at the velocity points (e.g., $u_{i+1/2,k}$, see Fig. 1). The variables defined in the water level points (e.g., $q_{i,k+1/2}$, $z_{i,k+1/2,}$ and ζ_i) are spatially interpolated by SWASH before output. Although with the second-order leapfrog scheme the time stamp of the velocities and water level and pressures differ by $\Delta t/2$ (e.g., $u^{n+1/2}_{i+1/2,k}$ and ζ^{n}_{i}), SWASH does not temporally interpolate variables before output. As the output time step Δt_{out} is usually much larger than the computational time step, this time difference is generally very small. As we adopted a minimum output time step of about 10 times the computational time step (see Section 3.3.1), we opted to truncate the results (i.e., assume that all output variables are at the same time stamp), rather than interpolating the output variables that differ by $10\Delta t$ to a time stamp of $\pm\Delta t/2$.

As we used equidistant vertical layers, we calculated the instantaneous depth-averaged velocities U_d as,

$$U^{n+1/2}_{d,i+1/2}=\frac{\sum_{k=1}^{k=K}u^{n+1/2}_{i+1/2,k}}{K}. \tag{B.21}$$

The discretization of the mass-flux and oscillatory velocities then reads,

$$U_{i+1/2}=\frac{\left\langle U^{n+1/2}_{d,i+1/2}\left(\overline{d_{i+1/2}}^{x}+\left(\overline{\zeta_{i+1/2}}^{x}\right)^{n+1}\right)\right\rangle}{\overline{d_{i+1/2}}^{x}+\left\langle\left(\overline{\zeta_{i+1/2}}^{x}\right)^{n+1}\right\rangle}, \tag{B.22}$$

$$\widetilde{u^{n+1/2}_{i+1/2,k}}=u^{n+1/2}_{i+1/2,k}-U_{i+1/2}, \tag{B.23}$$

The local acceleration term $\left\langle\frac{\partial\int_{-d}^{\zeta}\tilde{u}_i dz}{\partial t}\right\rangle$ is calculated with a backward difference scheme,

$$\frac{\frac{1}{k}\left\langle\sum_{k=1}^{k=K}\widetilde{u^{n+1/2}_{i+1/2}}\left(\overline{d_{i+1/2}}^{x}+\left(\overline{\zeta_{i+1/2}}^{x}\right)^{n+1}\right)-\sum_{k=1}^{k=K}\widetilde{u^{n+1/2-n^*}_{i+1/2}}\left(\overline{d_{i+1/2}}^{x}+\left(\overline{\zeta_{i+1/2}}^{x}\right)^{n+1-n^*}\right)\right\rangle}{\Delta t_{out}}, \tag{B.24}$$

with n* representing the time stamp difference of Δt_{out}.

The advective acceleration $(d+\langle\zeta\rangle)U_j\frac{\partial U_i}{\partial x_j}$ is calculated with a central difference scheme,

$$\left(\overline{d_{i+1/2}}^{x}+\left\langle\left(\overline{\zeta_{i+1/2}}^{x}\right)^{n+1}\right\rangle\right)U_{i+1/2}\frac{U_{i+3/2}-U_{i-1/2}}{2\Delta x}. \tag{B.25}$$

Note that as we adopted constant grid sizes and as we output the variables at every grid, the spatial derivatives are calculated with Δx.

The pressure gradient $g(d+\langle\zeta\rangle)\frac{\partial\langle\zeta\rangle}{\partial x_i}$ is calculated with a central difference scheme,

$$g\left(\overline{d_{i+1/2}}^{x}+\left\langle\left(\overline{\zeta_{i+1/2}}^{x}\right)^{n+1}\right\rangle\right)\frac{\left\langle\left(\overline{\zeta_{i+3/2}}^{x}\right)^{n+1}\right\rangle-\left\langle\left(\overline{\zeta_{i-1/2}}^{x}\right)^{n+1}\right\rangle}{2\Delta x}. \tag{B.26}$$

The hydrodynamic reaction at the bottom $\langle q_{-d}\rangle\frac{\partial d}{\partial x_i}$ is calculated with a central difference scheme,

$$\left\langle\left(\overline{q_{-d,i+1/2}}^{x}\right)^{n+1}\right\rangle\frac{\overline{d_{i+3/2}}^{x}-\overline{d_{i-1/2}}^{x}}{2\Delta x}. \tag{B.27}$$

The radiation stress S_{xx} is calculated by,

$$S_{xx,i+1/2}=\frac{1}{K}\left\langle\sum_{k=1}^{k=K}\left(\widetilde{u^{n+1/2}_{i+1/2}}\right)^{2}\left(\overline{d_{i+1/2}}^{x}+\left(\overline{\zeta_{i+1/2}}^{x}\right)^{n+1}\right)\right\rangle+\frac{1}{K}\left\langle\left(\overline{d_{i+1/2}}^{x}+\left(\overline{\zeta_{i+1/2}}^{x}\right)^{n+1}\right)\sum_{k=0}^{k=K}g\left(\overline{\zeta_{i+1/2}}^{x}-\overline{z_{i+1/2,k}}^{x,z}+\overline{q_{i+1/2,k}}^{x,z}\right)^{n+1}\right\rangle-0.5\,g\left(\overline{d_{i+1/2}}^{x}+\left\langle\left(\overline{\zeta_{i+1/2}}^{x}\right)^{n+1}\right\rangle\right)^{2}. \tag{B.28}$$

As the vertical layers and non-hydrostatic pressure output are provided at the cell vertical edges, the vertical interpolation is done in the post-processing. The radiation stress gradient $\frac{\partial S_{ij}}{\partial x_j}$ is calculated with a central difference scheme,

$$\frac{S_{xx,i+3/2}-S_{xx,i-1/2}}{2\Delta x}. \tag{B.29}$$

The bottom friction is calculated with the Manning formula, given by,

$$gc_f^2\left\langle U^{n+1/2}_{d,i+1/2}\left|U^{n+1/2}_{d,i+1/2}\right|\frac{1}{\left(\overline{d_{i+1/2}}^{x}+\left(\overline{\zeta_{i+1/2}}^{x}\right)^{n+1}\right)^{1/3}}\right\rangle \tag{B.30}$$

with a Manning roughness coefficient c_f of 0.019 $m^{-1/3}s$.

The turbulent eddy viscosity $\nu_{t,i+1/2}$ - a water depth based mixing length model - is calculated with a central difference scheme,

$$\nu_{t,i+1/2}=\left(\overline{d_{i+1/2}}^{x}+\left(\overline{\zeta_{i+1/2}}^{x}\right)^{n+1}\right)^{2}\left|\frac{U^{n+1/2}_{d,i+3/2}-U^{n+1/2}_{d,i-1/2}}{2\Delta x}\right|. \tag{B.31}$$

Note that the turbulent eddy viscosity is included when the hydrostatic front approximation is activated in the breaking zone (i.e., for cases with a null non-hydrostatic pressure, see Smit et al., 2013).

The Reynolds stress gradient $\frac{\partial\left\langle\int_{-d}^{\zeta}\tau_{ij}dz\right\rangle}{\partial x_j}$ is calculated with a central-difference scheme,

$$\left\langle\frac{\left(\overline{d_{i+3/2}}^{x}+\left(\overline{\zeta_{i+3/2}}^{x}\right)^{n+1}\right)\left(\frac{U^{n+1/2}_{d,i+5/2}-U^{n+1/2}_{d,i+1/2}}{2\Delta x}\right)\nu_{t,i+3/2}}{2\Delta x}-\frac{\left(\overline{d_{i-1/2}}^{x}+\left(\overline{\zeta_{i-1/2}}^{x}\right)^{n+1}\right)\left(\frac{U^{n+1/2}_{d,i+1/2}-U^{n+1/2}_{d,i-3/2}}{2\Delta x}\right)\nu_{t,i-1/2}}{2\Delta x}\right\rangle. \tag{B.32}$$

References

Anderson, J., 1995. Computational Fluid Dynamics: The Basics with Applications. McGrawhill Inc, pp. 1–547. http://dx.doi.org/10.1017/CBO9780511780066, 1995.

Andrews, D.G., Mcintyre, M.E., 1978. An exact theory of nonlinear waves on a Lagrangian-mean flow. J. Fluid. Mech. 89, 609–646. http://dx.doi.org/10.1017/S0022112078002773.

Apotsos, A., Raubenheimer, B., Elgar, S., Guza, R.T., 2008. Wave-driven setup and alongshore flows observed onshore of a submarine canyon. J. Geophys. Res. 113 (C07025), http://dx.doi.org/10.1029/2007JC004514.

Benedet, L., List, J.H., 2008. Evaluation of the physical process controlling beach changes adjacent to nearshore dredge pits. Coast. Eng. 55, 1224–1236. http://dx.doi.org/10.1016/J.COASTALENG.2008.06.008.

Berkhoff, J.C.W., 1972. Computation of combined refraction — Diffraction. In: Coastal Engineering 1972. American Society of Civil Engineers, New York, NY, pp. 471–490. http://dx.doi.org/10.1061/9780872620490.027.

Bertin, X., de Bakker, A., van Dongeren, A., Coco, G., André, G., Ardhuin, F., Bonneton, P., Bouchette, F., Castelle, B., Crawford, W.C., Davidson, M., Deen, M., Dodet, G., Guérin, T., Inch, K., Leckler, F., McCall, R., Muller, H., Olabarrieta, M., Roelvink, D., Ruessink, G., Sous, D., Stutzmann, É., Tissier, M., 2018. Infragravity waves: From driving mechanisms to impacts. Earth-Sci. Rev. 177, 774–799. http://dx.doi.org/10.1016/J.EARSCIREV.2018.01.002.

Booij, N., Ris, R.C., Holthuijsen, L.H., 1999. A third-generation wave model for coastal regions: 1. Model description and validation. J. Geophys. Res. Ocean. 104, 7649–7666. http://dx.doi.org/10.1029/98JC02622.

Buckley, M., Lowe, R., Hansen, J., 2014. Evaluation of nearshore wave models in steep reef environments. Ocean Dyn. 64, 847–862. http://dx.doi.org/10.1007/s10236-014-0713-x.

Buckley, M.L., Lowe, R.J., Hansen, J.E., Van Dongeren, A.R., 2015. Dynamics of wave setup over a steeply sloping fringing reef. J. Phys. Oceanogr. 45, 3005–3023. http://dx.doi.org/10.1175/JPO-D-15-0067.1.

Chen, G., Kharif, C., Zaleski, S., Li, J., 1999. Two-dimensional Navier–Stokes simulation of breaking waves. Phys. Fluids 11, 121–133. http://dx.doi.org/10.1063/1.869907.

Conde-Frias, M., Otero, L., Restrepo, J.C., Ortiz, J.C., Ruiz, J., Osorio, A.F., 2017. Swash oscillations in a microtidal dissipative beach. J. Coast. Res. 336, 1408–1422. http://dx.doi.org/10.2112/JCOASTRES-D-16-00147.1.

Dalrymple, R.A., Rogers, B.D., 2006. Numerical modeling of water waves with the SPH method. Coast. Eng. 53, 141–147. http://dx.doi.org/10.1016/J.COASTALENG.2005.10.004.

Derakhti, M., Kirby, J.T., Shi, F., Ma, G., 2016. Wave breaking in the surf zone and deep-water in a non-hydrostatic RANS model. Part 2: Turbulence and mean circulation. Ocean Model. 107, 139–150. http://dx.doi.org/10.1016/j.ocemod.2016.09.011.

Feddersen, F., Clark, D.B., Guza, R.T., 2011. Modeling surf zone tracer plumes: 1. Waves, mean currents, and low-frequency eddies. J. Geophys. Res. Ocean. 116. http://dx.doi.org/10.1029/2011JC007210.

Feddersen, F., Guza, R.T., 2003. Observations of nearshore circulation: Alongshore uniformity. J. Geophys. Res. 108 (3006), http://dx.doi.org/10.1029/2001JC001293.

Feddersen, F., Guza, R.T., Elgar, S., Herbers, T.H.C., 1998. Alongshore momentum balances in the nearshore. J. Geophys. Res. Ocean 103, 15667–15676. http://dx.doi.org/10.1029/98JC01270.

Fiedler, J.W., Smit, P.B., Brodie, K.L., McNinch, J., Guza, R.T., 2018. Numerical modeling of wave runup on steep and mildly sloping natural beaches. Coast. Eng. 131, 106–113. http://dx.doi.org/10.1016/J.COASTALENG.2017.09.004.

Haller, M.C., Dalrymple, R.A., Svendsen, I.A., 2002. Experimental study of nearshore dynamics on a barred beach with rip channels. J. Geophys. Res. 107 (3061), http://dx.doi.org/10.1029/2001JC000955.

Hansen, J.E., Elias, E., List, J.H., Erikson, L.H., Barnard, P.L., 2013. Tidally influenced alongshore circulation at an inlet-adjacent shoreline. Cont. Shelf Res. 56, 26–38. http://dx.doi.org/10.1016/j.csr.2013.01.017.

Hansen, J.E., Janssen, T.T., Raubenheimer, B., Shi, F., Barnard, P.L., Jones, I.S., 2014. Observations of surfzone alongshore pressure gradients onshore of an ebb-tidal delta. Coast. Eng. 91, 251–260. http://dx.doi.org/10.1016/J.COASTALENG.2014.05.010.

Hansen, J.E., Raubenheimer, B., List, J.H., Elgar, S., 2015. Modeled alongshore circulation and force balances onshore of a submarine canyon. J. Geophys. Res. Ocean 120, 1887–1903. http://dx.doi.org/10.1002/2014JC010555.

Hirt, C.W., Nichols, B.D., 1981. Volume of fluid (VOF) method for the dynamics of free boundaries. J. Comput. Phys. 39, 201–225. http://dx.doi.org/10.1016/0021-9991(81)90145-5.

Kennedy, A.B., Chen, Q., Kirby, J.T., Dalrymple, R.A., 2000. Boussinesq modeling of wave transformation, breaking, and runup. I: 1D. J. Waterw. Port, Coastal, Ocean Eng. 126, 39–47. http://dx.doi.org/10.1061/(ASCE)0733-950X(2000)126:1(39).

Lam, D.C., Simpson, R., 1976. Centered differencing and the box scheme for diffusion convection problems. J. Comput. Phys. 22, 486–500. http://dx.doi.org/10.1016/0021-9991(76)90045-0.

Lesser, G.R., Roelvink, J.A., van Kester, J.A.T.M., Stelling, G.S., 2004. Development and validation of a three-dimensional morphological model. Coast. Eng. 51, 883–915. http://dx.doi.org/10.1016/J.COASTALENG.2004.07.014.

Lin, P., Liu, P.L.F., 1998. A numerical study of breaking waves in the surf zone. J. Fluid Mech. 359, 239–264. http://dx.doi.org/10.1017/S002211209700846X.

Long, J.W., Özkan Haller, H.T., 2005. Offshore controls on nearshore rip currents. J. Geophys. Res. 110 (C12007), http://dx.doi.org/10.1029/2005JC003018.

Longuet-Higgins, M.S., Stewart, R.W., 1962. Radiation stress and mass transport in gravity waves, with application to 'surf beats'. J. Fluid Mech. 13, 481–504. http://dx.doi.org/10.1017/S0022112062000877.

Longuet-Higgins, M.S., Stewart, R.w., 1964. Radiation stresses in water waves; a physical discussion, with applications. Deep Sea Res. Oceanogr. Abstr. 11, 529–562. http://dx.doi.org/10.1016/0011-7471(64)90001-4.

Lowe, R.J., Buckley, M.L., Altomare, C., Rijnsdorp, D.P., Yao, Y., Suzuki, T., Bricker, J.D., 2019. Numerical simulations of surf zone wave dynamics using Smoothed Particle Hydrodynamics. Ocean Model. 144, 101481. http://dx.doi.org/10.1016/j.ocemod.2019.101481.

Lowe, R.J., Leon, A.S., Symonds, G., Falter, J.L., Gruber, R., 2015. The intertidal hydraulics of tide-dominated reef platforms. J. Geophys. Res. Ocean 120, 4845–4868. http://dx.doi.org/10.1002/2015JC010701.

Ma, G., Shi, F., Kirby, J.T., 2012. Shock-capturing non-hydrostatic model for fully dispersive surface wave processes. Ocean Model. 43–44, 22–35. http://dx.doi.org/10.1016/J.OCEMOD.2011.12.002.

Mei, C.C., Stiassnie, M., Yue, D.K.-P., 2005. Theory and Applications of Ocean Surface Waves, Journal of Fluid Mechanics, Advanced Series on Ocean Engineering. World Scientific, http://dx.doi.org/10.1142/5566.

Monaghan, J.J., 1994. Simulating free surface flows with SPH. J. Comput. Phys. 110, 399–406. http://dx.doi.org/10.1006/jcph.1994.1034.

Murphy, A.H., 1988. Skill scores based on the mean square error and their relationships to the correlation coefficient. Mon. Weather Rev. 116, 2417–2424. http://dx.doi.org/10.1175/1520-0493(1988)116<2417:SSBOTM>2.0.CO;2.

Nicolae Lerma, A., Pedreros, R., Robinet, A., Sénéchal, N., 2017. Simulating wave setup and runup during storm conditions on a complex barred beach. Coast. Eng. 123, 29–41. http://dx.doi.org/10.1016/j.coastaleng.2017.01.011.

Nwogu, O., 1993. Alternative form of Boussinesq equations for nearshore wave propagation. J. Waterw. Port, Coastal, Ocean Eng. 119, 618–638. http://dx.doi.org/10.1061/(ASCE)0733-950X(1993)119:6(618).

Peregrine, D.H., 1967. Long waves on a beach. J. Fluid Mech. 27, 815–827. http://dx.doi.org/10.1017/S0022112067002605.

Rijnsdorp, D.P., Ruessink, G., Zijlema, M., 2015. Infragravity-wave dynamics in a barred coastal region, a numerical study. J. Geophys. Res. Ocean. 120, 4068–4089. http://dx.doi.org/10.1002/2014JC010450.

Rogers, J.S., Monismith, S.G., Feddersen, F., Storlazzi, C.D., 2013. Hydrodynamics of spur and groove formations on a coral reef. J. Geophys. Res. Ocean 118, 3059–3073. http://dx.doi.org/10.1002/jgrc.20225.

Rooijen, A., Lowe, R., Rijnsdorp, D.P., Ghisalberti, M., Jacobsen, N.G., McCall, R., 2020. Wave-driven mean flow dynamics in submerged canopies. J. Geophys. Res. Ocean 125, 0–3. http://dx.doi.org/10.1029/2019JC015935.

Ruju, A., Lara, J.L., Losada, I.J., 2012. Radiation stress and low-frequency energy balance within the surf zone: A numerical approach. Coast. Eng. 68, 44–55. http://dx.doi.org/10.1016/j.coastaleng.2012.05.003.

Smagorinsky, J., 1963. General circulation experiments with the primitive equations. Mon. Weather Rev. 91, 99–164. http://dx.doi.org/10.1175/1520-0493(1963)091<0099:GCEWTP>2.3.CO;2.

Smit, P., Janssen, T., Holthuijsen, L., Smith, J., 2014. Non-hydrostatic modeling of surf zone wave dynamics. Coast. Eng. 83, 36–48. http://dx.doi.org/10.1016/j.coastaleng.2013.09.005.

Smit, P., Zijlema, M., Stelling, G., 2013. Depth-induced wave breaking in a non-hydrostatic, near-shore wave model. Coast. Eng. 76, 1–16. http://dx.doi.org/10.1016/j.coastaleng.2013.01.008.

Sous, D., Dodet, G., Bouchette, F., Tissier, M., 2020. Momentum balance across a barrier reef. J. Geophys. Res. Ocean http://dx.doi.org/10.1029/2019JC015503.

Stelling, G.S., Duinmeijer, S.P.A., 2003. A staggered conservative scheme for every froude number in rapidly varied shallow water flows. Internat. J. Numer. Methods Fluids 43, 1329–1354. http://dx.doi.org/10.1002/fld.537.

Stelling, G., Zijlema, M., 2003. An accurate and efficient finite-difference algorithm for non-hydrostatic free-surface flow with application to wave propagation. Internat. J. Numer. Methods Fluids 43, 1–23. http://dx.doi.org/10.1002/fld.595.

Stive, M.J.F., Wind, H.G., 1982. A study of radiation stress and set-up in the nearshore region. Coast. Eng. 6, 1–25. http://dx.doi.org/10.1016/0378-3839(82)90012-6.

Svendsen, I.A., 2005. Introduction to Nearshore Hydrodynamics. In: Advanced Series on Ocean Engineering, world scientific, http://dx.doi.org/10.1142/5740.

Wang, Z., Zou, Q., Reeve, D., 2009. Simulation of spilling breaking waves using a two phase flow CFD model. Comput. Fluids 38, 1995–2005. http://dx.doi.org/10.1016/J.COMPFLUID.2009.06.006.

Zijlema, M., 2019. The role of the rankine–hugoniot relations in staggered finite difference schemes for the shallow water equations. Comput. Fluids 104274. http://dx.doi.org/10.1016/J.COMPFLUID.2019.104274.

Zijlema, M., Stelling, G.S., 2005. Further experiences with computing non-hydrostatic free-surface flows involving water waves. Internat. J. Numer. Methods Fluids 48, 169–197. http://dx.doi.org/10.1002/fld.821.

Zijlema, M., Stelling, G.S., 2008. Efficient computation of surf zone waves using the nonlinear shallow water equations with non-hydrostatic pressure. Coast. Eng. 55, 780–790. http://dx.doi.org/10.1016/j.coastaleng.2008.02.020.

Zijlema, M., Stelling, G., Smit, P., 2011. SWASH: An operational public domain code for simulating wave fields and rapidly varied flows in coastal waters. Coast. Eng. 58, 992–1012. http://dx.doi.org/10.1016/j.coastaleng.2011.05.015.